HHS Public Access

Author manuscript

Cell Rep. Author manuscript; available in PMC 2025 January 09.

Published in final edited form as:

Cell Rep. 2024 November 26; 43(11): 114986. doi:10.1016/j.celrep.2024.114986.

Low-affinity ligands of the epidermal growth factor receptor are long-range signal transmitters in collective cell migration of epithelial cells

Eriko Deguchi[1], **Shuhao Lin**[2], **Daiki Hirayama**[2], **Kimiya Matsuda**[2], **Akira Tanave**[3,4], **Kenta Sumiyama**[3,4], **Shinya Tsukiji**[5], **Tetsuhisa Otani**[6,7], **Mikio Furuse**[7], **Alexander Sorkin**[8], **Michiyuki Matsuda**[1,2], **Kenta Terai**[1,9,10,*]

[1]Department of Pathology and Biology of Diseases, Graduate School of Medicine, Kyoto University, Yoshida-Konoe-Cho, Sakyo-ku, Kyoto 606-8501, Japan

[2]Research Center for Dynamic Living Systems, Graduate School of Biostudies, Kyoto University, Yoshida-Konoe-Cho, Sakyo-ku, Kyoto 606-8501, Japan

[3]Laboratory for Mouse Genetic Engineering, RIKEN Center for Biosystems Dynamics Research, 1-3 Yamadaoka, Suita, Osaka 565-0871, Japan

[4]Department of Animal Sciences, Graduate School of Bioagricultural Sciences, Nagoya University, Furo-cho, Chikusa, Nagoya 464-8601, Japan

[5]Department of Nanopharmaceutical Sciences, Nagoya Institute of Technology, Gokiso-cho, Showa-ku, Nagoya, Aichi 466-0061, Japan

[6]Laboratory of Cell Biology and Biochemistry, Department of Biological Sciences, Tokyo Metropolitan University, 1-1 Minami-Osawa, Hachioji 192-0397, Tokyo, Japan

[7]Division of Cell Structure, National Institute for Physiological Sciences, Okazaki, Aichi 444-8585, Japan

[8]Department of Cell Biology, School of Medicine, University of Pittsburgh, Pittsburgh, PA, USA

[9]Graduate School of Medicine, Tokushima University, Shinkura-cho, Tokushima 770-8501, Japan

[10]Lead contact

SUMMARY

*Correspondence: terai.kenta.5m@tokushima-u.ac.jp.

AUTHOR CONTRIBUTIONS

Conceptualization, methodology, validation, and formal analysis, E.D., M.M., and K.T.; investigation, E.D., S.L., and K.M.; data curation, E.D., M.M., and K.T.; resources, A.T., K.S., S.T., T.O., M.F., and A.S.; writing – original draft, E.D.; writing – review & editing, E.D., A.S., M.M., and K.T.; supervision, M.M. and K.T.; project administration, M.M. and K.T.; funding acquisition, E.D., M.M., and K.T.

DECLARATION OF INTERESTS

The authors declare no competing interest.

SUPPLEMENTAL INFORMATION

Supplemental information can be found online at https://doi.org/10.1016/j.celrep.2024.114986.

Canonical epidermal growth factor (EGF) receptor (EGFR) activation involves the binding of seven EGFR ligands (EGFRLs); however, their extracellular dynamics remain elusive. Here, employing fluorescent probes and a tool for triggering ectodomain shedding, we show that epiregulin (EREG), a low-affinity EGFRL, rapidly and efficiently activates EGFR in Madin-Darby canine kidney (MDCK) epithelial cells and mouse epidermis. During collective cell migration, EGFR and extracellular signal-regulated kinase (ERK) activation waves propagate in an a disintegrin and metalloprotease 17 (ADAM17) sheddase- and EGFRL-dependent manner. Upon induced EGFRL shedding, low-affinity ligands EREG and amphiregulin (AREG) mediate faster and broader ERK waves than high-affinity ligands. Tight/adherens junction integrity is essential for ERK activation propagation, suggesting that tight intercellular spaces prefer the low-affinity EGFRLs for efficient signal transmission. In EREG-deficient mice, ERK wave propagation and cell migration were impaired during skin wound repair. We additionally show that heparin-binding EGF-like growth factor (HBEGF) primarily promotes surrounding cell motility. Our findings underscore the pivotal role of low-affinity EGFRLs in rapid intercellular signal transmission.

Graphical abstract

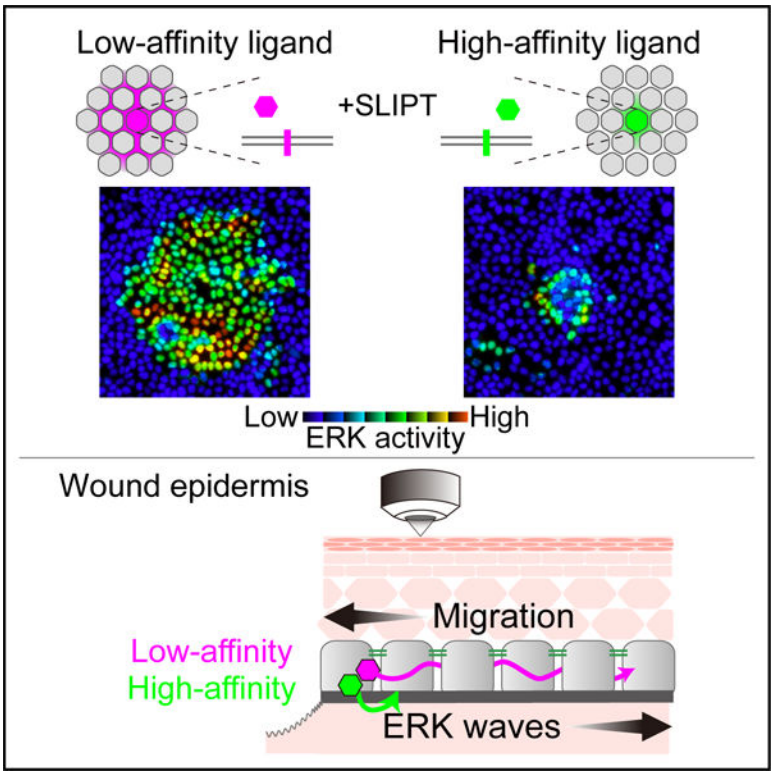

In brief

Deguchi et al. find that low-affinity EGFR ligands propagate faster and farther than high-affinity ligands in epithelial cells. They demonstrate that EREG, a low-affinity ligand, contributes to skin wound healing.

INTRODUCTION

The epidermal growth factor (EGF) receptor (EGFR)-Ras-extracellular signal-regulated kinase (ERK) signaling pathway governs a plethora of biological phenomena, encompassing cell proliferation, differentiation, and tumorigenesis.[1–3] The EGFR ligands (EGFRLs) comprise seven proteins and are categorized into two groups based on their receptor-binding affinity.[4] The high-affinity ligands, with apparent Kd values ranging from 0.1 to 1 nM, are EGF, transforming growth factor α (TGF-α), betacellulin (BTC), and heparin-binding EGF-like growth factor (HBEGF). In contrast, epiregulin (EREG), epigen (EPGN), and amphiregulin (AREG) are the low-affinity ligands, exhibiting affinities 10- to 100-fold lower than their high-affinity counterparts.[5] Recent investigations have illuminated that the receptor-binding affinity differentially stabilizes EGFR dimers and thereby plays a pivotal role in eliciting distinct cellular responses.[6,7] EGFRLs can also be categorized based on their sensitivity to sheddases,[8] their bioactivity in promoting cell growth and migration,[9,10] and their endocytic sorting.[11]

In addition to traditional fluorescently tagged EGFRLs, advanced probes have been developed to probe the characteristics of EGFRLs. First, the sensitivity to sheddases was examined by fusing peptide tags or alkaline phosphatase to the extracellular domain of EGFRLs.[8,12–14] Studies using these probes demonstrated that HBEGF, TGF-α, EREG, AREG, and EPGN, but not EGF or BTC, undergo shedding by a disintegrin and metalloprotease 17 (ADAM17). Second, fluorescent proteins have been fused to the C terminus of EGFRLs to investigate the intracellular trafficking of pro-EGFRLs.[15–18] Third, several groups have created probes by attaching fluorescent proteins to the extracellular domain of pro-EGFRLs.[19–21] While these probes were employed to monitor the cleavage efficiency of ADAM17, they did not provide insights into the extracellular dynamics of the shed EGFRL.

Notably, a substantial portion of current knowledge about the biological effects of individual EGFRLs is derived from experiments involving the bath application of recombinant EGFRLs to cultured cells. This approach, however, leaves unresolved questions concerning shedding, diffusion, and target cell activation within physiological contexts. A unique model system for investigating the physiological roles of EGFRLs is the collective cell migration exhibited by Madin-Darby canine kidney (MDCK) cells,[22] wherein recurrent waves of ERK activation propagate from the leader cells to the follower cells.[23–25] The propagation of these ERK activation waves, or simply ERK waves hereafter, has been shown to hinge upon ADAM17-mediated shedding of EGFRLs and intercellular mechanochemical force.[26,27] Later experiments demonstrated that all four EGFRLs expressed in MDCK cells—namely EGF, HBEGF, TGF-α, and EREG—collectively contribute to the ERK activation waves.[28] Meanwhile, MDCK cells express EGFR, ErbB2, and ErbB3, but not ErbB4. Among these, EGFR emerges as the predominant receptor, playing a critical role in the propagation of ERK waves.[29] Nevertheless, comprehensive analyses of individual EGFRLs have not been performed due to the absence of suitable probes for tracking EGFRLs and methods for inducing EGFRL shedding.

Here, we report our design of a series of EGFRL probes, named EGFRL-ScNeos, for visualization of the shedding and extracellular dynamics of individual EGFRLs. By using these probes in tandem with a chemical biology tool for eliciting EGFRL shedding, we elucidate distinctive characteristics inherent to each EGFRL. Remarkably, our observations reveal that EREG, one of the low-affinity EGFRLs, unexpectedly functions as a long-range signaling mediator, traversing the intercellular milieu beneath the tight/adherens junctions.

RESULTS

EGFRL-ScNeos visualize the shedding of EGFRLs and stimulate EGFR

We developed a series of seven dual-color fluorescent probes, EGFRL-ScNeos, to visualize the dynamics of the seven EGFRLs in live cells (Figures 1A and 1B). A probe for NRG1, a ligand for ErbB3 and ErbB4, was also developed according to the method in Kamezaki et al..[20] As the control, we employed the transmembrane protein Necl-5.[30]

We first evaluated the subcellular localization of EGFRL-ScNeos in confluent MDCK cells (Figure 1C). The cytoplasmic mNeonGreen signal localized to the plasma membrane, whereas extracellular mScarlet was observed in both the plasma membrane and the endosomes, suggesting that cleaved extracellular domains were engulfed and sorted to endosomes by EGFRL-ScNeo-producer cells or their neighbors. In the xz section, all probes localized primarily at the basolateral membrane and to a lesser extent at the apical membrane (Figure S1A). Expression levels of EGFRL-ScNeos were normalized by mNeonGreen intensity (Figure S1B). The relative cleavage efficiency was quantified by measuring fluorescence intensity (Figure 1D). Western blot analysis of cell lysates (Figure 1E) revealed uncleaved pro-EGFRLs in both anti-mScarlet and anti-mNeonGreen blots. Meanwhile, the cleaved cytoplasmic domain of EGFRLs was detected only in the anti-mNeonGreen blot. We assumed that minor bands are generated by incomplete cleavage of multiple protease-sensitive sites or glycosylation.[13,31,32] We estimated the fraction of cleaved probes based on the western blot (Figure 1F). Secretion of the cleaved EGFRL into the medium was also examined (Figure 1G). Then, we calculated EGFRL production rates (Figure 1H). In conclusion, TGF-α was most efficiently cleaved and secreted among the seven EGFRLs under basal conditions. Of note, growing cells on permeable supports did not significantly affect probe subcellular localization (Figure S1C).

Next, the ADAM17-dependent shedding of EGFRL-ScNeos was analyzed (Figures 1I, S1D, and S1E and Video S1). The mScarlet/mNeonGreen ratios of EREG, AREG, and EPGN, but not EGF, HBEGF, TGF-α, BTC, and NRG1, were significantly decreased by an ADAM17 stimulator, 12-O-tetradecanoylphorbol 13-acetate (TPA). The mScarlet/mNeonGreen ratios of all EGFRLs except for EGF and BTC were significantly increased by an inhibitor, marimastat. This observation is consistent with the previous reports that, except for EGF and BTC, EGFRLs are sensitive to ADAM17.[8] Although TPA is known to induce HBEGF shedding,[33] it did not decrease the mScarlet/mNeonGreen ratio of HBEGF. This could be due to either TPA altering the substrate specificity of ADAM17, as previously reported,[14] or cleaved HBEGF remaining bound through its heparin-binding domain, preventing a decrease in mScarlet fluorescence.

Finally, we investigated whether the cleaved EGFRL-ScNeos retained biological activity. For this purpose, each EGFRL-ScNeo was stably expressed in MDCK-4KO cells, which lack all four EGFRL genes expressed in MDCK cells, EGF, HBEGF, TGF-α, and EREG.[28] All culture supernatants from EGFRL-ScNeo-expressing MDCK-4KO cells transiently stimulated ERK (Figure 1J), although the level of maximum activation was different for each EGFRL (Figure 1K). We observed that HBEGF stimulated ERK most efficiently (Figure 1L). We obtained similar results by using recombinant EGFRLs (Figure S1F), indicating that the mScarlet-tagged EGFRLs retained the biological activity. This observation was also confirmed by immunoblotting with the anti-phospho-EGFR antibody (Figure S1G). Thus, we concluded that EGFRL-ScNeos retain their biological activity and reflect the dynamics of EGFRLs.

EGFRL-ScNeo highlights short- and long-range EGFRLs

Using EGFRL-ScNeos, we addressed the question of how far each EGFRL travels toward the surrounding cells after being shed from the producer cells (Figure 2A). The mScarlet signal was used to track each EGFRL (Figures 2B–2D). As expected, the signal was not observed in cells surrounding the Necl5-ScNeo-expressing cells, whereas mScarlet signals were detected up to 80 μm from HBEGF-ScNeo-expressing producer cells. To a lesser extent, mScarlet signals were detected around cells expressing NRG1-ScNeo, EGF-ScNeo, and AREG-ScNeo. The signals were fainter in cells surrounding the producer cells of TGF-α, EREG, and BTC, probably reflecting the lower EGFR affinity or lower cleavage rates. The signals were below the quantifiable level in cells surrounding EPGN-producer cells, presumably reflecting the low affinity to the EGFR. The mScarlet signals in the receiver cells were abolished when ADAM17 was eliminated from the producer cells, confirming that the signals were derived from ADAM17-cleaved EGFRL-ScNeo (Figure S2).

We then examined how EGFR binding affects EGFRL distribution by using Erbock cells, in which all four ErbB-family receptors are knocked out[29] (Figure 2E). While at first look, mScarlet signals for HBEGF and NRG1 appeared not significantly changed, tangential images revealed HBEGF accumulation at the basal surface of Erbock cells (Figure 2F), suggesting that HBEGF binds to heparan sulfate proteoglycans (HSPGs) in parental MDCK cells. In accordance with this hypothesis, the HSPG inhibitor surfen significantly suppressed the mScarlet signal in receiver cells surrounding HBEGF producer cells (Figure 2G).

Next, cellular uptake of EGFRL by the receiver cells was quantified by flow cytometry (Figure 2H). When producer and receiver cells were co-cultured at a ratio of 1:1, more than 50% of the receivers were scored as mScarlet positive with the probes for EGF, HBEGF, TGF-α, BTC, and NRG1, which are classified as high-affinity ligands. At a co-culture ratio of 1:10, more than 50% of HBEGF- and TGF-α-receiver cells were still mScarlet positive, but this percentage decreased markedly at co-culture ratios of 1:100 and 1:400; only receiver cells of the HBEGF probe had a significant mScarlet-positive population under these ratios. This result implies that TGF-α was diluted to below the detection limit, whereas HBEGF reached a limited number of cells over a short distance and thus retained a strong signal.

Low-affinity EGFRLs diffuse faster and farther than high-affinity EGFRLs

The above experiments investigated the distribution of EGFRLs in the absence of stimulation, i.e., constitutive cleavage by the basal sheddase activity. Here, we examined the EGFRL dynamics upon acute ADAM17 activation by self-localizing ligand-induced protein translocation (SLIPT). Briefly, the synthetic myristoyl-D-Cys-tethered TMP (m^{D}cTMP) triggers translocation of cytoplasmically expressed cRaf to the plasma membrane,[34] activating ADAM17 through the ERK pathway. To validate this system, we introduced *Escherichia coli* dihydrofolate reductase (eDHFR)-cRaf into TSen-expressing cells, a fluorescence resonance energy transfer (FRET) probe for ADAM17[35] (Figure 3A). As anticipated, upon the addition of m^{D}cTMP, ADAM17 was activated in a dose-dependent manner (Figure 3B). We expressed AREG-ScNeo with miRFP703-eDHFR-cRaf and observed its decrease in the mScarlet/mNeonGreen ratio upon m^{D}cTMP addition (Figure 3C and Video S2), indicating that acute ADAM17 activation caused AREG shedding.

Next, we visualized how shed EGFRL activates EGFR in the surrounding receiver cells by measuring ERK activity using the EKARrEV FRET biosensor (Figure 3D). Note that the effect of endogenous EGFRLs was eliminated in this assay because both producer and receiver cells lacked endogenous EGFRLs. m^{D}cTMP triggered ERK activation waves from cells producing EREG, AREG, TGF-α, HBEGF, and NRG1, but not from EGF, BTC, and EPGN producers (Figures 3E, 3F, and S3 and Video S3). We suppose that the difference in the amplitude of ERK activation between Figures 1K and 3F reflects different stimulation methods, namely bath application versus inducible shedding. The lack of response of EPGN was likely due to a low uncleaved level before stimulation (Figure S1D), while EGF and BTC agreed with the insensitivity to ADAM17 inhibitor (Figure S1E). The essential role of ADAM17 in producer cells, but not receiver cells, was confirmed using ADAM17-deficient MDCK cells (Figure S2). Low-affinity ligands EREG and AREG showed ERK wave velocities of ~4 μm min^{-1}, approximately four times faster than the high-affinity ligands HBEGF and TGF-α at 1–2 μm min^{-1} (Figures 3G and 3H). ERK-activated area was also larger for low-affinity ligands, though not significantly so in AREG (Figure 3I). Producer cells secreted similar amounts of high- and low-affinity EGFRLs (Figures 3J and 3K), and neither cell density in receiver cells (Figures S4A–S4C) nor initial ligand amounts (Figures S4D and S4E) significantly affected ERK activation dynamics. These observations suggest that in the confluent epithelial cell layer, low-affinity EGFRLs transmit signals faster to distant cells than high-affinity EGFRLs.

In EGFR-deficient cells, the ERK activation wave was abolished when the producer cells expressed AREG, TGF-α, or HBEGF; partially suppressed with EREG; and unaffected with NRG1 (Figure S4F). These results demonstrate that EGFR serves as the primary receptor mediating the ERK wave propagation in MDCK cells, aligning with our previous study.[29] In the latter two producer-cell lines, further deletion of ErbB3 and ErbB4 eliminated the ERK waves (Figure S4G). These observations are consistent with the previous reports showing the binding of EREG and NRG1 to ErbB3 and ErbB4.[9] We confirmed that the SLIPT system triggers EGFRL shedding via ADAM17 (Figure S4H). We found no significant difference in the velocity of ERK waves between the probes with or without extracellular mScarlet (Figures S4I and S4J). Cell-cell traction force contributes to ERK waves during collective

cell migration[26]; however, we did not find any effect on m^{D}cTMP-stimulated ERK waves by actin polymerization perturbation (Figure S4K), indicating that ERK activation propagation was primarily mediated by EGFRL diffusion.

The affinity and density of EGFR regulate the diffusion of EGFRLs in the intercellular space

Why do the ERK waves by the low-affinity EGFRLs propagate faster than those by the high-affinity EGFRLs? Among the high-affinity EGFRLs, TGF-α uniquely sorted to the basolateral membrane in a Naked2-dependent manner.[36] To examine whether the cytoplasmic domain affects ERK wave velocity, we generated a TGF-α-EREG chimera (Figure 4A). We found that ERK wave velocity induced by the TGF-α-EREG chimera was comparable to that of authentic TGF-α, supporting the notion that high affinity to EGFR underlies the slow wave propagation (Figure 4B). Based on this, we examined whether the density of EGFR on the plasma membrane may also affect the ERK wave velocity. Indeed, overexpression of human EGFR in receiver cells slowed down EREG-induced ERK waves to the level of HBEGF-induced ERK waves (Figure 4C). Thus, in the tight intercellular spaces, EGFRLs are rapidly sequestered depending on the affinity to and the density of EGFR.

What happens when the intercellular barrier is perturbed? α−1-catenin (*CTNNA1*) deletion abolished ERK wave propagation for all ligands except HBEGF (Figure 4D and Video S4), despite not affecting growth factor sensitivity.[26] While HBEGF remains functional due to HSPG sequestration, adherens junctions are essential for other ERK waves. Disrupting tight junctions in claudin quintuple knockout (quinKO) cells[37] significantly reduced EREG-induced wave propagation, though not completely (Figure 4E). In contrast, E-cadherin or p120-catenin knockout (KO) had no significant impact on ERK waves, indicating that these proteins are not essential for maintaining EREG within intercellular compartments (Figure 4F). Since only *CTNNA1*-deficient cells lost both apicobasal polarity and tight-junction formation (Figure S5), EREG signal propagation appears to require both tight junctions and sealing by claudin.

To confirm that EREG mediates rapid ERK wave propagation in endogenous expression, we introduced eDHFR-cRaf into wild-type (WT), EREG knockout (dEREG), 4KO, and EGF/HBEGF/TGFα triple knockout (TKO) MDCK cells.[28] As expected, rapid ERK activation was observed in EREG-expressing WT and TKO cells, but not in dEREG and 4KO cells (Figures 4G and 4H). In short, within the confined space bounded by the tight/adherens junction, basolateral plasma membrane, and basal membrane, high-affinity EGFRLs are efficiently sequestered by EGFR on the plasma membrane, allowing low-affinity EGFRLs to diffuse faster than high-affinity EGFRLs.

HBEGF but not EREG drives migration of confluent MDCK cells

To investigate the effect of each EGFRL on collective cell migration, we used the previously reported ‘‘boundary assay.’’[26] We formed the boundary between the two cell populations: producer cells expressing EGFRL with eDHFR-cRaf and receiver cells expressing a FRET biosensor (Figure 5A). Upon m^{D}cTMP addition, ERK waves propagated from the boundary

to receiver cells (Figure 5B and Video S5). We found that only HBEGF induced receiver cells to migrate against the ERK wave direction (Figure 5C). Soluble HBEGF promotes MDCK cell migration, though its difference from other EGFRLs remains unclear.[38] Signaling molecules other than ERK could cause this difference.[39] Examining tyrosine kinases and ROCK activities using Picchu[40] and Eevee-ROCK FRET biosensors[41] revealed faster activation waves with EREG than with HBEGF (Figure 5D and Video S6). We then reasoned that ERK activation patterns may explain the difference in cell migration induction. EREG triggered fast ERK wave propagation with a short delay between neighboring cells, while HBEGF produced a distance-dependent peak shift of ERK activation and approximately two times larger ERK wave duration (Figures 5E and 5F). Thus, the delay and/or duration of the signal may cause a difference in induced cell migration.

HBEGF, but not EREG, is sorted to lysosomes

EGFR signaling strength is known to be regulated by sorting after activation.[11,42] Thus, we tracked EGFRLs after shedding and stained with early and late endosome markers (Figure 6A). Consistent with a previous report,[11] EREG localized to both early and late endosomes, whereas HBEGF localized more to late endosomes (Figures 6B and 6C). Since HBEGF and EREG bind to ErbB4, we also used Erbock-ErbB1 cells, which express only human EGFR (Figures 6D and 6E). Again, HBEGF localized to late endosomes more efficiently than EREG. Thus, EGFRL-EGFR binding affinity appears to affect the fate of the EGFRL-EGFR complex within the cells and may affect subsequent biological outcome.

EREG is required for collective cell migration of wounded mouse epidermis

The above results motivated us to intensively investigate how ligand expression affects collective cell migration in MDCK cells. As we reported previously,[28] the retardation of wave amplitude and velocity was marginal in EREG or HBEGF KO cells (Figure 7A). To quantitatively analyze wave propagation from the wound edge, we used a kymograph with a wider view field, covering 2,225 μm along the wound edge over a longer observation period (Figures 7B and S6A). The reduced ERK wave propagation distance in both EREG and HBEGF KO cells suggests that EGFRLs exhibit functional redundancy in collective cell migration, consistent with previous studies (Figure 7C).

However, each KO displayed distinct characteristics. EREG-deficient cells showed diminished ERK wave amplitude, indicating impaired wave synchronization, which may have resulted in compromised long-range ERK activity propagation. Consistent with our hypothesis that ERK waves drive collective cell migration, EREG-deficient cells showed reduced cell migration velocity after 10 h (Figures 7D, 7E, and S6B). Surprisingly, HBEGF KO elevated basal ERK activity in follower cells and prolonged the initial ERK activation wave, while disrupting stripe ERK wave patterns after 10 h (Figures 7B and S6A). This might lead to more pronounced migration defects compared with dEREG cells (Figures 7B, 7E, S6A, and S6B). Since HBEGF has strong and sustained ERK activation capacity, as shown in Figures 1K and 5E, its loss may disrupt the negative feedback system.

ERK waves may play a role in epidermal cell migration during mouse skin wound healing.[25,27] In HBEGF-deficient mice, a statistically significant delay in wound healing

was reported on days 7 and 8.[43] However, no statistically significant delay was reported in EREG-deficient mice.[44] Therefore, to re-evaluate the function of EREG-mediated ERK waves, we also generated EREG-KO mouse lines expressing an ERK FRET biosensor[45] (Figure S6C). The mice were born with Mendelian ratios and did not show any abnormality to the detectable level, in agreement with the previous report.[44] In their study, Shirasawa et al.[44] concluded that EREG plays no significant role in mouse skin wound healing, based on their full-thickness skin excision model, including epidermis, dermis, and subcutaneous tissue. To examine epidermal cell migration, we applied a shallow incision, less than 100 μm deep, through the epidermis and upper dermis only (Figure S6D). We observed the auricular epidermis after wounding using two-photon microscopy as described previously (Figure 7F).[25] Repeated waves of ERK activation were generated from the wound edge in both WT and *Ereg*$^{-/-}$ mice (Figure 7G). However, the waves were extinguished at 200 μm or less in *Ereg*$^{-/-}$ mice, whereas the waves reached more than 800 μm in the WT (Figures 7H and S6E and Video S7). Furthermore, the epidermal cells located more than 200 μm from the wound edge migrated less efficiently in *Ereg*$^{-/-}$ mice than in WT mice (Figures 7I and S6F). Thus, we concluded that EREG serves as a long-range signal transmitter during skin wound healing.

DISCUSSION

Among the four EGFRLs expressed in MDCK cells, EREG, the lowest-affinity EGFRL, plays a major role in the propagation of ERK activation to distant cells. Intuitively, the low-affinity EGFRLs reach more distant cells than do the high-affinity EGFRLs, because they are less likely to be trapped by EGFR. However, because the low affinity dampens the efficiency of EGFR activation, we cannot foresee whether the low-affinity EGFRLs transmit signals more efficiently to distant cells than the high-affinity EGFRLs. Lauffenburger and colleagues elegantly demonstrated, by theoretical and experimental approaches, that decreased affinity of EGF to EGFR could increase the distance of signal propagation.[46,47] However, it has not been demonstrated in which physiological contexts the low affinity becomes an advantage for the EGFRLs. We found that the requirements are at least the intactbarrier segregating the intercellular space from the apical space (Figures 4D and 4E) as well as a physiological level of EGFR expression (Figure 4C). Such conditions could occur at least in the skin because EREG KO perturbed the migration of epidermal cells located distant from the wound edge (Figure 7I). The narrow space segregated by the tight/adherens junction and basement membrane of the epidermis may render the low affinity an advantageous property. The requirement of EREG for epithelial regeneration was also reported in the bronchiolar epithelium[48] and intestinal mucosa.[49] In both cases, activated fibroblasts are the source of EREG; therefore, the mechanism responsible for maintaining a high concentration of EREG in the bronchiolar epithelium and intestinal mucosa may be different from that in the epidermis, but we anticipate that in all these cases the mechanism involves a restriction of the diffusion of EREG *in vivo*.

EGF is an archetype of paracrine factors, but the spatial range that EGF and other EGFRLs shed from a single cell could influence remains elusive even in tissue culture cells. The EGFRL-ScNeo probes allow us to challenge these questions. We need to consider at least three properties of EGFRLs: shedding, diffusion, and affinity to EGFR. In our

present experiments, we found that TGF-α is most efficiently cleaved in the steady state (Figure 1H) due to its high sensitivity to metalloproteases (Figures 1D–1F).[50] In agreement with this finding, Bunker et al. reported that the surface expression of TGF-α is almost undetectable in the absence of a metalloprotease inhibitor.[21] Due to the high sensitivity to metalloproteases and high affinity to EGFR, TGF-α is efficiently engulfed by essentially all cells in a culture dish (Figure 2B). This observation also indicates that, unlike EREG, TGF-α is efficiently released to the luminal side through tight/adherens junctions. It was reported that MDCK cells cultured on permeable supports, but not on plastic dishes, shed most of the TGF-α to the basolateral side.[50] However, we failed to find significant differences in the distribution of TGF-α between the permeable supports and the cover glasses used to plate MDCK cells (Figure S1C).

In contrast to TGF-α, HBEGF was heavily accumulated inside the neighboring cells (Figures 2B and 2H). When EGFR-deficient cells were used, HBEGF was accumulated at the basal surface of the neighboring cells (Figure 2F), indicating that HBEGF is trapped by the HSPGs on the cell surface. Treatment with surfen, which prevents growth factors from binding to HSPGs, notably reduced the mScarlet signal in receiver cells surrounding the HBEGF producer cell (Figure 2G). Therefore, the HBEGF cleaved by metalloproteases is bound to the surface of neighboring cells through HSPGs and then taken up in an EGFR-dependent manner. In line with this view, we found that only HBEGF could activate ERK in the α−1-catenin KO cells surrounding the HBEGF-producer cells (Figure 4D and Video S4). This property may also underpin previous observations that HBEGF functions as a juxtacrine growth factor.[51,52] In this context, juxtacrine does not mean that the pro-HBEGF remaining uncleaved as a membrane integral protein functions to stimulate EGFR. Our observation indicates that the shed HBEGF stimulates preferentially adjacent cells simply because HSPGs decelerate HBEGF diffusion.

Why does HBEGF but not EREG induce cell movement in the boundary assay (Figures 5A–5C)? Reciprocal cycles of increase in traction force and ERK activation are the engine of collective cell migration of MDCK cells.[22] The pulling force of the leader cells stretches the follower cells to activate EGFR and, thereby, ERK. The activated ERK not only reorganizes the actomyosin network to generate traction force but also activates ADAM17 to shed EGFRLs. EGFRLs and the pulling force cooperatively activate EGFR on the adjacent cell to ignite another cycle. To make this scenario operate, the optimal time delay between each step is critical. During collective cell migration of MDCK cells, the increase in traction force is followed by ERK activation with a 2 min delay.[26] ERK activation is followed by accumulation of phosphorylated myosin light chain with a 6 min delay.[24] It takes 7 min for an ERK wave to pass through a single cell.[22] This delay enables cells to move in a peristaltic manner. An analysis using optogenetic tools found that ERK activity waves at a velocity of 2.0–3.0 μm/min are optimal for driving MDCK cells.[24] The velocity of the ERK activity wave generated by HBEGF, 1.0 μm/min, is slower than the optimal value (Figure 3H), but this may be within a permissible range because the ERK wave velocity in mouse epidermis is 1.4 μm/min[25] Meanwhile, EREG-generated waves propagating at 4 μm/min may be moving too fast to drive MDCK cell movements.

Other factors that might have caused the phenotypical difference between HBEGF and EREG are the duration of ERK activation and the different sorting pathways after binding to EGFR. With respect to the first factor, the full width at half-maximum (FWHM) of ERK waves upon HBEGF shedding was approximately 2-fold larger than that upon EREG shedding (Figure 5F). In support of this finding, in the case of migration of MCF7 driven by bath application of EGF, a low dose, but not a high dose, of EGF can induce cell migration because of sustained ERK activation.[42] It has been reported that different ligands undergo different endocytic sorting.[11] In line with this, we found that HBEGF but not EREG was sorted into late endosomes (Figure 6). Thus, the intracellular signaling pathways may differ between HBEGF and EREG. This issue should be examined in future studies.

If HBEGF is the primary driver of cell migration, what role does EREG play? In both MDCK cells and wounded mouse epidermal cells, stochastic ERK activation is frequently observed.[23,25] Following EGFR activation, cells enter a refractory phase. The rapid propagation of EREG may facilitate the entrainment of Distance from leader cell ERK activation, helping decaying waves reach distant cells. This mechanism could explain why EREG deficiency reduces the propagation distance of ERK waves in both tissue culture cells (Figures 4G, 4H, 7B, 7C, and S6A) and mouse skin (Figures 7F–7H and S6E).

Chemogenetic tools are widely used to perturb intracellular signaling cascades, but much less frequently used to untangle intercellular communications. Here, we employed the SLIPT system to activate ADAM17,[34] thereby shedding EGFRLs. This approach will also be useful for studying the effects of other ADAM17 target molecules such as tumor necrosis factor α (TNF-α). On the other hand, this method is not specific, in that all targets of ERK will be activated in cells with the SLIPT system and all ADAM17 target molecules will be cleaved. The cleavage of the ADAM17 target is not necessarily dependent only on ADAM17. For example, cleavage of EGFRLs is also regulated by iRhoms.[53,54] ERK is known to activate ADAM17,[55] but other kinases can also modulate ADAM-family metalloproteases,[14,56] raising a question about the specificity. Moreover, we failed to activate ADAM10 in MDCK cells, which prevented us from studying the roles of EGF and BTC. This should be overcome in the future.

Our experimental system, which features the EGFRL producer surrounded by receivers, closely resembles the apoptotic-cell-induced radial ERK waves that prevent apoptosis in surrounding cells and accelerate epithelial cell sealing.[57,58] Gagliardi et al.[57] demonstrated that EGFR, MMP, and EGFRLs mediate the apoptosis-induced ERK wave propagation and concluded against the free diffusion of EGFRLs by using MCF10A cells cultured on a microfluidic system. However, EREG diffuses through narrow spaces beneath a tight junction, an area unaffected by fluid flow over the cells. Therefore, we propose that diffusion of EREG may contribute to ERK wave propagation in the apoptosis-derived ERK activity propagation.

In conclusion, we have revealed that low-affinity EGFRLs propagate ERK activation faster and further *in vitro* and *in vivo*. Our findings will shed light on the importance of low-affinity ligands in cell-to-cell communication in the physiological context, thus bringing us closer to understanding the significance of the existence of multiple EGFRLs.

Limitations of the study

Although we have identified the shared role of EREG in both basal layer and MDCK cell lines, it would be a context-dependent function. Indeed, the expression level of EGFR alters the diffusion constant of EREG (Figure 4C). In addition, microenvironments such as basement membrane stiffness and intercellular communication with other cells may affect the function of EREG. Further, *in vivo* studies may be essential to validate our findings. The effect of fusion proteins has not been thoroughly tested partly due to the availability of antibodies against EGFRLs. The subcellular distribution, sensitivity to ADAM17, and biological effect as the EGFR agonist of the EGFRLs-ScNeos generally agree with previous reports, but further examination will be required. We failed to induce the cleavage of EGF-ScNeo and BTC-ScNeo, which are expected to be substrates of ADAM10. We applied calcium ionophore or other stimuli that are reported to activate ADAM10, but we did not observe any changes in the fluorescence ratio. In addition, our analysis of endocytic sorting is limited to the use of early and late endosome markers. We attempted to employ potential recycling endosomal markers, but none proved functional in MDCK cells. The detailed mechanisms by which differences in endocytic sorting influence signaling and migration require further investigation in future studies.

STAR★METHODS

RESOURCE AVAILABILITY

Lead contact—Requests for further information and resources should be directed to and will be fulfilled by the lead contact, Kenta Terai (terai.kenta.5m@tokushima-u.ac.jp).

Materials availability—Plasmids generated in this study have been deposited with Addgene. The plasmid numbers are listed in the key resources table. Mouse lines generated in this study have been deposited with the Laboratory Animal Resource Bank, National Institutes of Biomedical Innovation, Health and Nutrition. The resource numbers are listed in the key resources table. All unique/stable reagents generated in this study are available from the lead contact without restriction.

Data and code availability

- Microscopy data and original immunoblot images collected for this study have been deposited with the Systems Science of Biological Dynamics repository (SSBD: repository) and are publicly available as of the date of publication. The DOI is listed in the key resources table.
- This study does not report the original code.
- Any additional information required to reanalyze the data reported in this paper is available from the lead contact upon request.

EXPERIMENTAL MODEL AND STUDY PARTICIPANT DETAILS

Mouse strains—The B6N Albino-*Ereg*$^{-/-}$ Tg (hyBRET-ERK-NLS) pT2A-6011NLS (or simply, *Ereg*$^{-/-}$ hyBRET-ERK-NLS) were developed using a CRISPR/Cas9 system targeting the murine Ereg gene (NC_000071.6). Three Alt-R™ CRISPR-Cas9 crRNAs

were co-injected with Alt-R™ CRISPR-Cas9 tracrRNA and Alt-R™ S.p. Cas9 Nuclease V3 (Integrated DNA Technologies, Inc.) into the cytoplasm of the fertilized eggs obtained from C57BL/6N hyBRET-ERK-NLS mice[45] as reported.[64] The crRNA sequences are listed in the key resources table. 7- to 9-week-old male mice were used for the *in vivo* imaging. No statistical methods were used to predetermine sample size. The experiments were not randomized. The investigators were not blinded to allocation during experiments and outcome assessment. The animal protocols were approved by the Animal Care and Use Committee of Kyoto University Graduate School of Medicine (approval nos. 22063, 23049). The experiments were carried out under the relevant regulations. The study is compliant with all relevant ethical regulations regarding animal research.

Cell lines—MDCK and Lenti-X 293T cells were provided by RIKEN BioResource Center (no. RCB0995) and Clontech (no. 632180), respectively. MDCK II and Claudin quinKO cells were reported.[37] Cells were cultured in DMEM (no. 044–29765; Wako) with 10% (vol/vol) FBS (no. F7524; Sigma-Aldrich), 100 units mL^{-1} penicillin, and 100 μg mL^{-1} streptomycin (no. 26253–84; Nacalai Tesque) in cell culture dishes at 37°C and 5% CO2 in a humidified incubator.

METHOD DETAILS

Plasmids—The plasmids are listed in the key resources table. Some cDNAs were synthesized by GeneArt (Thermo Fisher Scientific): pro-EREG (NCBI CCDS database no. CCDS3564.1), pro-AREG (NCBI CCDS database no. CCDS3565.1), pro-EPGN (NCBI CCDS database no. CCDS59478.1), pro-NRG1 (NCBI CCDS database no. CCDS6083.1), pro-BTC (NCBI CCDS database no. CCDS3566.1), and mNeonGreen.[65] The cDNA of mScarlet[60] was obtained from Addgene (Addgene no. 85042). Expression plasmids for EGFRL-ScNeo were constructed using PCR. For TGFα, the last 6 nucleotides were modified to encode valines required for intracellular trafficking.[66,67] To generate TGFα-EREG chimera, TGFα (1–123 a.a.) and EREG (140–169 a.a.) were fused directly. The cDNAs encoding EGFRL-ScNeos were subcloned into the pCSII vector[68] and pPB vector.[61] The cDNA of Necl5-ScNeo was obtained from the previously established plasmid pPBbsr2-Necl5-ScNeo (Addgene no. 170283).[30]

Reagents and antibodies—The reagents are listed in the key resources table. m^{D}cTMP was synthesized in previous report.[59] The following primary and secondary antibodies with the dilution buffer were used for immunoblotting: anti-mCherry (1:1,000); anti-mNeonGreen (1:1,000); anti-phospho-EGFR (Tyr1068) (1:1,000); anti-alpha Tubulin (1:1,000); IRDye 680-conjugated (1:10,000); and IRDye 800CW (1:10,000).

The following primary and secondary antibodies with the dilution buffer were used for immunofluorescence: anti-GP135 (1:100); anti-ZO-1 (1:100); anti-EEA1 (1:250); anti-Rab7 (1:100); anti-RFP (1:500); AMCA-conjugated (1:25); Cy5-conjugated (1:250); Alexa 405-conjugated (1:250); Alexa 647-conjugated (1:100); Alexa 546-conjugated (1:500).

Establishment of stable cell lines—A lentiviral expression system was employed to establish MDCK cells[26,28] stably expressing EGFRL-ScNeo. Briefly, for the preparation of

the lentivirus, pCSII vector,[68] psPAX2 (Addgene Plasmid: no. 12260), and pCMV-VSV-G-RSV-Rev[68] were co-transfected into Lenti-X 293T cells by using polyethyleneimine (no. 24765–1; Polyscience Inc.). MDCK cells were incubated with the lentivirus and after 2 days of incubation, the cells were treated with 2 μg mL^{-1} puromycin, 10 μg mL^{-1} blasticidin S or 100 μg mL^{-1} zeocin for the selection. The cells were sorted using a FACS Aria IIu cell sorter (Becton Dickinson) with mNeonGreen fluorescence to achieve a uniform expression level of the EGFRL-ScNeo. MDCK cells stably expressing EGFRL-ScNeo, miRFP703-eDHFR(69K6)-cRaf, TSen, human EGFR, or tyrosine kinase biosensor were established with a piggyBac transposon system. pPB plasmids and pCMV-mPBase(neo-) encoding piggyBac transposase[61] were co-transfected into MDCK cells by electroporation with an Amaxa nucleofector (Lonza), followed by selection with 2 μg mL^{-1} puromycin, 10 μg mL^{-1} blasticidin S or 100 μg mL^{-1} zeocin. MDCK cells expressing EKARrEV-NLS,[28] EKAREV-NLS,[62] and Eevee-ROCK-NES[26] were reported.

CRISPR/Cas9-mediated KO cell lines—For CRISPR/Cas9-mediated KO of genes encoding EGFRLs, ErbB receptors, ADAM17, α−1-catenin, E-cadherin, and p120-catenin, single guide RNAs (sgRNA) targeting the exons were designed[27–29] using CRISPRdirect[69]. The gRNA sequences are listed in the key resources table. Oligonucleotide DNAs for the sgRNA were cloned into lentiCRISPRv2[70] (Addgene no. 52961), pX458[71] (Addgene no. 48138), or pX459[71] (Addgene no. 62988) vectors. The expression plasmids for sgRNA and Cas9 were introduced into MDCK cells by lentiviral infection (for lentiCRISPRv2) or electroporation (for pX458 and pX459) as described above. The mutations were validated by immunoblotting or DNA sequencing.

Fluorescence imaging with a confocal laser microscope—Cells were observed with a Leica TCS SP8 FALCON confocal microscope (Leica-Microsystems) equipped with an HC PL APO 40x/1.30 OIL CS2 objective, an HC PL APO 63x/1.40 OIL CS2 objective, Lecia HyD SMD detectors, a white light laser of 80 MHz pulse frequency, a Diode 405 (VLK 0550 T01; LASOS), a 440 nm diode laser (PDL 800-D; PicoQuant), and a stage top incubator (Tokai Hit) to maintain 37°C and 5% CO2. The following excitation wavelengths and emission band paths were used for the imaging: for CFP and YFP imaging, 440 nm excitation, 467–499 nm and 520–550 nm emission, respectively; for mNeonGreen imaging, 505 nm excitation, 515–560 nm emission; for mScarlet imaging, 569 nm excitation, 579–650 nm emission; for miRFP imaging, 670 nm excitation, 680–800 nm emission; for Alexa 405 imaging, 405 nm excitation, 415–500 nm emission; for Alexa 546 imaging, 561 nm excitation, 570–640 nm emission; for Alexa 647 imaging, 650 nm excitation, 660–750 emission. To eliminate the background signal, the time gate for mScarlet and miRFP fluorescence detection was set from 0.5 ns to 6.5 ns and 0.3 ns to 6.0 ns, respectively.

Time-lapse imaging with wide-field fluorescence microscopes—Wide-field fluorescence images were acquired following our established protocol[72]. Briefly, cells cultured on glass-bottom plates (Matsunami Glass) were observed under an ECLIPSE Ti2 inverted microscope (Nikon) equipped with a 10X/0.30 PlanFluor, a 20X/0.70 S Plan Fluor LWD ADM, a 40X/0.60 S Plan Fluor ELWD ADM, an ORCA Fusion Digital CMOS camera (Hamamatsu Photonics K.K.), an X-Cite TURBO LED light source (Excelitas

Technologies), a Perfect Focus System (Nikon), a TI2-S-SE-E motorized stage (Nikon), and a stage top incubator (Tokai Hit) to maintain 37°C and 5% CO2. The following filters were used for the time-lapse imaging: for CFP and YFP imaging, a 434/32 excitation filter (Nikon), a dichroic mirror 455 (Nikon), and 480/40 and 535–30 emission filters (Nikon) for CFP and YFP, respectively; for mScarlet imaging, a 570/40 (Nikon) excitation filter, a dichroic mirror 600 (Nikon), and a 645/75 emission filter (Nikon); for miRFP703 imaging, an FF01–640/14 excitation filter (Semrock), a dichroic mirror 660 (Nikon), and a 700/75 emission filter (Nikon).

Image processing for the FRET/CFP ratio—Image processing for FRET/CFP ratio images was performed with Fiji.[63] The background intensity was subtracted by using the subtract-background function and subsequently processed with a median filter to reduce noise. The processed images were subjected to image calculation and the ratio values were binned into 8 steps to obtain 8-color FRET/CFP ratio images. To convey the brightness of the original images to the FRET/CFP ratio images, the 8-color FRET/CFP ratio images were multiplied by the corresponding intensity-normalized grayscale image.

Fluorescence imaging of EGFRL-ScNeo—2.0×10^4 MDCK-EGFRL-ScNeo cells were seeded on a 96-well glass-bottom plate coated with 0.3 mg mL^{-1} type I collagen. The medium was replaced with DMEM with 10% FBS on Day 1 and observed on Day 2 under a TCS SP8 microscope at a resolution of 0.045 μm/pixel using a 63x/1.40 NA objective, 505 nm excitation for 1.5% and 569 nm for 2.0% of a white light laser, and HyD SMD detectors for 515–560 nm and 579–650 nm for gain of 60%, respectively.

Western blot analysis of EGFRL-ScNeo—5.0×10^5 MDCK-EGFRL-ScNeo cells were plated in a 6-well plate. One day after seeding, cells were lysed with SDS sample buffer. All antibodies were diluted in Odyssey blocking buffer (LI-COR Biosciences). Proteins were detected by an Odyssey Infrared Imaging System (LI-COR Biosciences). Cleaved/total pro-EGFRL was calculated by dividing the sum of the intensities of mNeonGreen bands corresponding to the cleaved form by the sum of the total mNeonGreen bands.

Quantification of EGFRL in the culture supernatant—2.5×10^6 MDCK-4KO-EGFRL-ScNeo cells were plated in a 10 cm dish. One day after seeding, cells were washed with PBS and the medium was replaced with DMEM without FBS. After 24h incubation, the medium was collected and centrifuged at 200 g for 3 min. mScarlet levels were quantified by Western blot with anti-mCherry antibody.

For the calibration of mScarlet, ArcticExpress (DE3) Competent Cells were transformed with pRSETB-mScarlet. The samples were separated by SDS-PAGE. The gel was stained with CBB, and the amount of mScarlet in the sample was calculated using a standard curve of BSA.

Analysis of ADAM sensitivity—For the time-lapse imaging of EREG-ScNeo, 4.0×10^4 MDCK-EREG-ScNeo cells were seeded on a 96-well glass-bottom plate coated with 0.3 mg mL^{-1} type I collagen. The medium was DMEM with 10% FBS. One day after seeding, cells

were observed under a TCS SP8 microscope at a resolution of 0.18 μm/pixel using a 63x/1.40 NA objective, 505 nm excitation for 2.5% and 569 nm for 4.0% of a white light laser, and HyD SMD detectors for 515–560 nm and 579–650 nm for gain of 60%, respectively. During observation, 10 nM TPA or 10 μM Marimastat was added. mScarlet/mNeonGreen ratio images were generated using the Fiji plug-in. Pseudo-color ratio images were generated by multiplying 8-color mScarlet/mNeonGreen images with the corresponding grayscale images.

For the quantification of the mScarlet/mNeonGreen ratio of EGFRL-ScNeo, 2.0×10^4 MDCK-EGFRL-ScNeo cells were seeded on a 96-well glass-bottom plate. The medium was DMEM with 10% FBS. For ADAM activation, one day after seeding, cells were observed under a TCS SP8 microscope at a resolution of 0.18 μm/pixel using a 63x/1.40 NA objective, 505 nm excitation for 4.0% and 569 nm for 6.0% of a white light laser, and HyD SMD detectors for 515–560 nm and 579–650 nm for gain of 60%, respectively. During observation, 10 nM TPA was added. For ADAM inhibition, 3 h after seeding, cells were supplemented with 10 μM Marimastat or 0.1% DMSO. One day after seeding, cells were observed under a TCS SP8 microscope at a resolution of 0.28 μm/pixel using a 40x/1.30 NA objective, 505 nm excitation for 0.7% and 569 nm for 1.0% of a white light laser, and HyD SMD detectors for 515–560 nm and 579–650 nm for gain of 60%, respectively.

Analysis of ERK activation by the supernatant of EGFRL-ScNeo—To collect supernatants from EGFRL-ScNeo-expressing cells, 2.0×10^4 MDCK-4KO-EGFRL-ScNeo cells were seeded in a 96-well plate. 5 h after seeding, cells were washed with PBS and the medium was replaced with Medium 199. After 20 h, the supernatant was collected. The number of ligand molecules in the supernatant was normalized with the amount of mScarlet by Western blot with anti-mCherry antibody.

For the detection of ERK activity by live imaging, 1.0×10^4 MDCK-4KO-EKARrEV-NLS cells were seeded on a 96-well glass-bottom plate coated with 0.3 mg mL^{-1} type I collagen. One day after seeding, the medium was replaced with Medium 199. After 2 h, cells were observed under an ECLIPSE Ti2 microscope. During observation, the medium was replaced with supernatants of MDCK-4KO-EGFRL-ScNeo or MDCK-4KO-EKARrEV-NLS. Image processing for FRET/CFP ratio images was performed with Fiji following our established protocol.[28] Briefly, cells were tracked using the Fiji TrackMate plugin[73] to measure the time course of the FRET/CFP ratio in each cell. The time-series data of the coordinates of each cell and the FRET/CFP ratio representing ERK activity were processed by using MATLAB. The FRET/CFP ratio in each cell was normalized with the average FRET/CFP ratios of 12 timepoints before the replacement of supernatants.

For the detection of phospho-EGFR level by Western blot, 2.0×10^4 MDCK-4KO-EKARrEV-NLS cells were seeded on a 96-well glass-bottom plate coated with 0.3 mg mL^{-1} type I collagen. One day after seeding, the medium was replaced with Medium 199. After 48 h, the medium was replaced with supernatants of MDCK-4KO-EGFRL-ScNeo or MDCK-4KO-EKARrEV-NLS. 10 minutes after the medium change, cells were lysed with SDS buffer, followed by Western blot with anti-phospho-EGFR antibody. For the controls

of the experiment, MDCK-4KO-EKARrEV-NLS cells were supplemented with EGF 10 ng mL^{-1} for 10 min or Trametinib 200 nM for 30 min.

Flow cytometry analysis of EGFRL-ScNeo—MDCK-EGFRL-ScNeo cells suspended in PBS containing 3% FBS were analyzed with a FACS Aria IIu cell sorter (Becton Dickinson). The following combinations of lasers and emission filters: For the detection of mNeonGreen fluorescence, a 488-nm laser and a DF530/30 filter (Omega Optical) were used. Cells were gated for size and granularity to exclude cell debris and aggregates. Data analysis was performed using FlowJo software (Tree Star).

Co-culture experiment of EGFRL-ScNeo—1.0×10^2 MDCK-EGFRL-ScNeo cells were mixed with 4.0×10^4 parental MDCK, MDCK-Erbock#5, or MDCK-dErbB1#1 cells and seeded on a 96-well glass-bottom plate coated with 0.3 mg mL^{-1} type I collagen. One day after seeding, the medium was replaced with Medium 199. The cells were observed under a TCS SP8 microscope at a resolution of 0.57 μm/pixel using a 40x/1.30 NA objective, 505 nm excitation for 1.5% and 569 nm for 8.0% of a white light laser, and HyD SMD detectors for 515–560 nm for gain of 80% and 579–650 nm for gain of 150%. Z stack images were acquired every 1 μm for 21 slices.

For quantification of mScarlet signals around producer-cells, the following commands of Fiji were applied sequentially on mScarlet and mNeonGreen z stack images: ‘‘Median…,’’ ‘‘radius=3 stack,’’ ‘‘Z Project…,’’ ‘‘projection=[Average Intensity]’’. For making ROIs on producer-cells, the mNeonGreen images were further processed as follows: ‘‘Make Binary,’’ with Li method, ‘‘Open,’’ ‘‘Dilate’’. For quantification of surrounding mScarlet signals, the ROI was dilated every 5 pixels, and the difference in mScarlet intensities between ROIs was measured. mScarlet intensities were normalized with mNeonGreen intensities of producer-cells. Then the square root of the normalized mScarlet intensities was plotted against the distance from the first ROI. For the calculation of the distance to reach the detectable mScarlet threshold, approximate curves were set from the first five points in the mScarlet decay curve.

The 3D image reconstruction was performed by using Volocity software (PerkinElmer).

For the administration of surfen, HBEGF-ScNeo cells co-cultured with WT MDCK cells. 3 h after seeding, cells were supplemented with 0.1% DMSO or 5 μM surfen, and maintained for one day under the condition. Cells were then observed under a TCS SP8 microscope.

Flow cytometry analysis of co-culture experiments—MDCK-EGFRL-ScNeo cells and parental MDCK cells were mixed at a cell number ratio of 1:1 to 1:400 in total 2.0×10^5 cells and seeded on a 12-well plate (no. 150628; Thermo Fisher Scientific). One day after seeding, cells suspended in PBS containing 3% FBS were analyzed with a FACS Aria IIu cell sorter.

Fluorescence imaging of TSen—4.0×10^4 cells expressing miRFP703-eDHFR(69K6)-cRaf were seeded on a 96-well glass-bottom plate coated with 0.3 mg mL^{-1} type I collagen. One day after seeding, the medium was replaced with Medium 199. After 2 h, cells were

observed under a TCS SP8 microscope at a resolution of 0.18 μm/pixel using a 63x/1.40 NA objective, 440 nm excitation of a diode laser, and HyD SMD detectors for 467–499 nm and 520–550 nm for gain of 80%, respectively. During observation, m^{D}cTMP was added to 0.01 to 10 μM or 0.1% DMSO.

Shedding of EGFRL and observation of ERK activity by SLIPT—MDCK-4KO-EGFRL-ScNeo cells or MDCK-EKARrEV-NLS cells with or without EGFRL gene knockout expressing miRFP703-eDHFR(69K6)-cRaf were used as the producer-cells. MDCK-EKARrEV-NLS cells with or without gene knockout of ErbB receptors or adherens junction molecules, or MDCK II-EKARrEV-NLS cells, Claudin quinKO-EKARrEV-NLS cells, MDCK-5102HRasCT(Picchu) cells, and MDCK-Eevee-ROCK-NES cells were used as the receiver cells. For the SLIPT assay, 1.0×10^{2} producer cells were mixed with 8.0×10^{4} receiver cells and seeded on a 96-well glass-bottom plate coated with 0.3 mg mL^{-1} type I collagen. 3 h after seeding, the medium was replaced with DMEM with 1% BSA. One day after seeding, the medium was replaced with Medium 199. After 2 h, cells were imaged under an ECLIPSE Ti2 microscope or a TCS SP8 microscope. For the ECLIPSE Ti2 microscope, a 20X/0.70 NA or 40X/0.60 NA objective was used at a resolution of 1.3 μm/pixel or 0.65 μm/pixel, respectively. For the TCS SP8 microscope, a 40x/1.30 OIL CS2 objective was used at a resolution 0.76 μm/pixel, 440 nm excitation of a diode laser, and HyD SMD detectors for 467–499 nm for gain of 80% and 520–550 nm for gain of 40%, respectively. During observation, 10 μM m^{D}cTMP was added.

Analysis of SLIPT-induce EGFRL in the culture supernatant—Subconfluent MDCK-4KO-EGFRL-ScNeo cells expressing eDHFR-cRaf were washed with PBS and replaced with Medium 199. After 1h incubation, the medium was replaced with fresh medium. Following another 1h incubation, the medium was collected as a non-stimulation condition and then replaced with fresh medium containing 10 μM m^{D}cTMP. After 1 h incubation with m^{D}cTMP, the medium was collected as a stimulation condition. Supernatants were mixed with SDS sample buffer, separated by SDS-PAGE. The amount of mScarlet in each sample was detected by Western blot with anti-mCherry antibody.

Boundary assay—Cells were seeded and observed under microscopy following our established protocol.[26] Briefly, MDCK-4KO-EGFRL-ScNeo cells expressing miRFP703-eDHFR(69K6)-cRaf were seeded in a well of a Culture-Insert 2 well (ibidi) placed. After incubation, the insert was removed, and MDCK-4KO-EKARrEV-NLS cells were plated around the EGFRL-producing cells with 10 μM Marimastat. After 2 h, cells were washed with PBS to remove the EGFRL-receiver-cell aggregates on EGFRL-producer-cell, and the medium was replaced with Medium 199 with 10 μM Marimastat and 10% FBS. After 16 h, the interface between EGFRL-producer-cells and MDCK-4KO-EKARrEV-NLS cells was imaged, and 10 μM m^{D}cTMP was added. The Fiji TrackMate plugin was applied to the CFP fluorescence images to track each cell over 10 h after treatment with m^{D}cTMP to determine cell displacement.

Analysis of ERK activity and FWHM of ERK activation in each receiver cell—The velocity of the radial ERK activity wave was analyzed using MATLAB as described in

the below section, and time-series data of the FRET/CFP ratio and distance from the center were obtained. Time-series data of the FRET/CFP ratio for 10 cells from the center were plotted against time for HBEGF and EREG, respectively. For quantification of the FWHM of ERK activation, the time required for ERK activation to recover to the half-maximum value was calculated. The half-maximum was defined as the average of the ratio value before EGFRL secretion (basal) and just after adding m^{D}cTMP (maximum) in each receiver cell.

Fluorescence imaging of the endocytic pathway—For co-immunofluorescence of EEA1 and Rab7 in MDCK-4KO cells, 1.0×10^2 MDCK-4KO-EREG-ScNeo or MDCK-4KO-HBEGF-ScNeo cells expressing miRFP703-eDHFR(69K6)-cRaf were mixed with 8.0×10^4 MDCK-4KO cells and seeded on a μ-Plate 96-Well Black (ibidi). Cells were supplemented with 10 μM Marimastat. One day after seeding, cells were imaged at a resolution of 0.20 μm/pixel under a spinning-disk confocal Marianas system based on the Zeiss Axio Observer Z1 inverted fluorescence microscope and CSU-W1 spinning disk, equipped with 405-, 445-, 488-, 515-, 561-, and 640-nm lasers, a 633/1.4 NA oil immersion objective, an Evolve electron-multiplying charge-coupled device camera, and piezo-controlled z-step motor, all controlled by SlideBook 6 software (Intelligent Imaging Innovation). Typically, a z-stack of 20 x–y confocal images was acquired at 0.4 μm steps. During observation, m^{D}cTMP was added to 10 μM. After 75 min, cells were fixed in freshly prepared 4% PFA for 30 min, permeabilized in 0.1% Triton X-100 in calcium- and magnesium-free (CMF)-PBS/0.1% BSA for 10 min, and then incubated for 1 h at RT with anti-EEA1 mouse antibody (1:250) and anti-Rab7 rabbit antibody (1:100) in CMF-PBS/0.1% BSA. EEA1 antibody was detected using a secondary anti-mouse antibody conjugated with AMCA (1:25). Rab7 antibody was detected using a secondary anti-rabbit antibody conjugated with Cy5 (1:250).

For co-immunofluorescence of EEA1 and Rab7 in MDCK-Erbock#5 cells, 1.0×10^2 MDCK-4KO-EREG-ScNeo or MDCK-4KO-HBEGF-ScNeo cells expressing miRFP703-eDHFR(69K6)-cRaf were mixed with 4.0×10^4 MDCK-Erbock#5 cells expressing EGFR and seeded on a 96-well glass-bottom plate coated with 0.3 mg mL^{-1} type I collagen. Cells were supplemented with 10 μM Marimastat. One day after seeding, cells were imaged under the TCS SP8 microscope at a resolution of 0.10 μm/pixel using a 63x/1.40 NA objective, 569 nm excitation for 10% and 650 nm for 10% of a white light laser, and HyD SMD detectors for 579–640 nm and 660–750 nm for gain of 500%, respectively. Typically, a z-stack of 40–50 x–y confocal images was acquired in 0.3 μm steps. During observation, m^{D}cTMP was added to 10 μM. After 60 min, cells were fixed in freshly prepared 4% PFA for 30 min, permeabilized in 0.1% Triton X-100 in calcium- and magnesium-free (CMF)-PBS/0.1% BSA for 10 min, and then incubated for 1 h at RT with anti-EEA1 mouse antibody (1:100) and anti-Rab7 rabbit antibody (1:100) and anti-RFP rat antibody (1:500) and in CMF-PBS/0.1% BSA. EEA1 antibody was detected using Alexa 405-conjugated goat anti-mouse IgG (H+L) antibody (1:250). Rab7 antibody was detected using Alexa 647-conjugated goat anti-rabbit IgG (H+L) antibody (1:100). RFP antibody was detected using Alexa 546-conjugated goat anti-rat IgG (H+L) antibody (1:500).

Measurement of the fraction of mScarlet-EGFRL colocalized with EEA1 or Rab7—3D images of cells were smoothed using a Gaussian filter with sigma of 1.0 pixels by Fiji. A segment mask was generated from background-subtracted images to select voxels detected through the 561-nm or 579-nm channel (total mScarlet-EGFRL). Additional segment masks were generated to include all voxels detected through the 640-nm or 660-nm channel (Mask-Rab7), and to include all voxels detected through the 405-nm channel (Mask-EEA1). For all masks, identical threshold parameters were used for experimental variables. A ‘‘colocalization’’ mask was then generated to select voxels overlapping between the total mScarlet-EGFRL mask and Mask-Rab7 or Mask-EEA1. The sum fluorescence intensity of the 561- or 579-nm channel in the colocalization mask was divided by the sum fluorescence intensity of the mScarlet-EGFRL in each FOV to calculate the fraction of total cellular mScarlet-EGFRL co-localized with EEA1 or Rab7.

Confinement release assay—The confinement release assay was performed following our established protocol.[26] Briefly, to observe the collective cell migration of MDCK cells, a Culture-Insert 2 Well (ibidi) was placed on a 35 mm glass-base dish (IWAKI) coated with 0.3 mg mL^{-1} type I collagen. 8.75×10^4 MDCK cells were then seeded in the Culture-Insert. 24 h after seeding, the silicone confinement was removed, and the medium was replaced with Medium 199. Beginning at 30 min after the removal of the silicone confinement, the cells were imaged with an epifluorescence microscope every 5 min. To determine cell displacement, the Fiji TrackMate plugin was applied to the CFP fluorescence images to track each cell from 10 to 22 h after the initiation of migration.

Analysis of ERK activation waves with kymographs—The FRET/CFP ratio images were cropped to obtain regions with a length of 2225 μm along the y-axis. Heat maps of ERK activity were obtained by interpolating the signals in regions between the nuclei of MDCK cells in the FRET/CFP ratio images. These values were then averaged along the y-axis in a defined region of the images, providing an intensity line along the x-axis. This operation was repeated for the respective time points, and the intensity lines were stacked along the y-axis for all time points. The ERK activation waves were detected after binarizing by Fiji. We manually delineated lines along the ERK activation waves and measured their length along the x-axis for quantification of ERK activity wave propagation subsequent to 10 h post-wounding.

Genotyping of *Ereg* KO mice by quantitative PCR—Genomic DNAs from the fingers of wild-type (WT) and *Ereg* KO mice were prepared, and then subjected to qPCR analysis for genotyping of the mice with primers (Table S1). The absolute abundance of each target site was calculated using a standard curve obtained from WT genomic DNA. The amounts of target sites were normalized by the internal control, *Tbp*.[74] When the amount of any of the three target sites was less than 0.5% compared to the WT, the genotype was considered a KO. Some PCR products were sequenced.

Time-lapse *in vivo* two-photon imaging of the wounded ear skin of mice—The *in vivo* imaging was performed following our established protocol.[25,45] Briefly, 18 h before the start of the imaging, mice were anesthetized with 1.5% isoflurane (Abbot Japan), the ear

hair was removed, and a surgical scalpel was used to create epithelial wounds on the ear skin. Then, 2P excitation microscopy was performed with an FV1200MPE-IX83 inverted microscope equipped with a 330/1.05 NA silicon oil-immersion objective lens (UPLSAPO 30XS; Evident), an InSight DeepSee Ultrafast laser (Spectra-Physics), an IR cut filter (BA685RIF-3; Evident), two dichroic mirrors (DM505 and DM570; both from Evident), and two emission filters (BA460–500 for CFP and BA520–560 for YFP; both from Evident). The interval of the z-stack imaging was set at 1 μm. Kymographs depicting ERK activity were created via a customized MATLAB script. The Fiji TrackMate plugin was used to track each cell's displacement for 3 h based on CFP fluorescence images.

QUANTIFICATION AND STATISTICAL ANALYSIS

mScarlet/mNeonGreen ratio of EGFRL-ScNeo and FRET/CFP ratio of TSen— For quantification of the mScarlet/mNeonGreen ratio at the plasma membrane of EGFRL-ScNeo, the following commands were applied sequentially using Fiji on mNeonGreen images: ''8- bit,'' ''Make Binary,'' ''Watershed,'' ''Open,'' ''Close-,'' and ''Analyze Particles…,'' ''size=1-Infinity circularity=0.00–0.60'' for making ROIs on the cell membrane. Intensities of mScarlet and mNeonGreen in each ROI were measured to calculate mScarlet/mNeonGreen ratio. The FRET/CFP ratio at the plasma membrane of TSen expressing cells was quantified using ROIs on CFP images following the same commands as described above.

The velocity of the ERK activity wave—The velocity was analyzed using MATLAB (MathWorks) as described with a modification.[25] First, on the CFP image, nuclei were automatically recognized with a segmentation program. Second, the FRET/CFP values of each nucleus were smoothed with the Savitzky–Golay filter by 20-min moving averages. Third, for each nucleus of the receiver cells, the distance from the center was plotted against the peak time. Then the velocity of ERK propagation was approximated by a linear model.

The radius of the ERK activity wave—The radius was analyzed using Python as described with a modification.[75] Ratio images of MDCK cells expressing EKARrEV-NLS were created after background subtraction. A median filter and a Gaussian 2D filter were applied to each image for noise reduction. The ratio image was normalized by a minimum intensity projection along the time axis. The processed images were binarized with a predetermined threshold and processed by morphological opening and closing to refine the ERK-activated area. Center coordinates and equivalent circle radii were obtained from each ERK-activated area. The maximum radius of the equivalent circle was defined as the radius of the ERK activity wave.

The receiver-cell density—The density in each producer-cell population, images of nuclei (EKARrEV-NLS) were analyzed to count nuclei within a 100 μm radius from producer-cells using the Fiji plug-in. On CFP images, the following commands were applied sequentially: ''8- bit,'' ''Subtract Background…'' with a rolling ball radius of 50 pixels, ''Make Binary,'' with Otsu method, ''Watershed,'' and ''Analyze Particles…'' with ''size=10-Infinity circularity=0.08–1.00'' for counting cell nuclei in each image.

The number of producer-cells—We manually counted the number of producer-cells at the time of shedding induction with m^{D}cTMP, using images of miRFP703-eDHFR(69K6)-cRaf expressed in producer-cells.

The depth of cutaneous wounds—The depth from the skin surface to the bottom of the wounds was measured manually in Imaris ver9.9.1 (Bitplane).

Statistical analysis—All statistical analyses were carried out using Microsoft Excel software (Microsoft). Probability (p) values were determined by using the T.TEST function of Microsoft Excel with two-tailed distribution and two-sample unequal variance. The sample number for this calculation (n) is indicated in each figure legend.

Supplementary Material

Refer to Web version on PubMed Central for supplementary material.

ACKNOWLEDGMENTS

We are grateful to the members of the Matsuda Laboratory for their helpful input; to K. Hirano, T. Uesugi, and K. Takakura, who provided technical assistance; and to the Medical Research Support Center of Kyoto University. This work was supported by the Kyoto University Live Imaging Center. Financial support was provided by JSPS KAKENHI grants (21H05226 and 21H02715 to K.T. and 19H00993 and 20H05898 to M.M.), a JST Moonshot R&D grant (JPMJMS2022 to M.M.), NIH grants (GM148363 and CA089151 to A.S.), and a JST SPRING grant (JPMJSP2110 to E.D.).

REFERENCES

1. Nishida E, and Gotoh Y (1993). The MAP kinase cascade is essential for diverse signal transduction pathways. Trends Biochem. Sci 18, 128–131. 10.1016/0968-0004(93)90019-j. [PubMed: 8388132]
2. Yarden Y, and Sliwkowski MX (2001). Untangling the ErbB signalling network. Nat. Rev. Mol. Cell Biol 2, 127–137. 10.1038/35052073. [PubMed: 11252954]
3. Linggi B, and Carpenter G (2006). ErbB receptors: new insights on mechanisms and biology. Trends Cell Biol 16, 649–656. 10.1016/j.tcb.2006.10.008. [PubMed: 17085050]
4. Harris RC, Chung E, and Coffey RJ (2003). EGF receptor ligands. Exp. Cell Res 284, 2–13. 10.1016/s0014-4827(02)00105-2. [PubMed: 12648462]
5. Jones JT, Akita RW, and Sliwkowski MX (1999). Binding specificities and affinities of egf domains for ErbB receptors. FEBS Lett 447, 227–231. 10.1016/s0014-5793(99)00283-5. [PubMed: 10214951]
6. Freed DM, Bessman NJ, Kiyatkin A, Salazar-Cavazos E, Byrne PO, Moore JO, Valley CC, Ferguson KM, Leahy DJ, Lidke DS, and Lemmon MA (2017). EGFR ligands differentially stabilize receptor dimers to specify signaling kinetics. Cell 171, 683–695.e18. 10.1016/j.cell.2017.09.017. [PubMed: 28988771]
7. Hu C, Leche CA, Kiyatkin A, Yu Z, Stayrook SE, Ferguson KM, and Lemmon MA (2022). Glioblastoma mutations alter EGFR dimer structure to prevent ligand bias. Nature 602, 518–522. 10.1038/s41586-021-04393-3. [PubMed: 35140400]
8. Sahin U, Weskamp G, Kelly K, Zhou HM, Higashiyama S, Peschon J, Hartmann D, Saftig P, and Blobel CP (2004). Distinct roles for ADAM10 and ADAM17 in ectodomain shedding of six EGFR ligands. J. Cell Biol 164, 769–779. 10.1083/jcb.200307137. [PubMed: 14993236]
9. Wilson KJ, Gilmore JL, Foley J, Lemmon MA, and Riese DJ. (2009). Functional selectivity of EGF family peptide growth factors: implications for cancer. Pharmacol. Ther 122, 1–8. 10.1016/j.pharmthera.2008.11.008. [PubMed: 19135477]
10. Singh B, Carpenter G, and Coffey RJ (2016). EGF receptor ligands: recent advances. F1000Res 5, 2270. 10.12688/f1000research.9025.1.

11. Roepstorff K, Grandal MV, Henriksen L, Knudsen SLJ, Lerdrup M, Grøvdal L, Willumsen BM, and van Deurs B (2009). Differential effects of EGFR ligands on endocytic sorting of the receptor. Traffic 10, 1115–1127. 10.1111/j.1600-0854.2009.00943.x. [PubMed: 19531065]
12. Tokumaru S, Higashiyama S, Endo T, Nakagawa T, Miyagawa JI, Yamamori K, Hanakawa Y, Ohmoto H, Yoshino K, Shirakata Y, et al. (2000). Ectodomain shedding of epidermal growth factor receptor ligands is required for keratinocyte migration in cutaneous wound healing. J. Cell Biol 151, 209–220. 10.1083/jcb.151.2.209. [PubMed: 11038170]
13. Hinkle CL, Sunnarborg SW, Loiselle D, Parker CE, Stevenson M, Russell WE, and Lee DC (2004). Selective roles for tumor necrosis factor alpha-converting enzyme/ADAM17 in the shedding of the epidermal growth factor receptor ligand family: the juxtamembrane stalk determines cleavage efficiency. J. Biol. Chem 279, 24179–24188. 10.1074/jbc.M312141200. [PubMed: 15066986]
14. Dang M, Armbruster N, Miller MA, Cermeno E, Hartmann M, Bell GW, Root DE, Lauffenburger DA, Lodish HF, and Herrlich A (2013). Regulated ADAM17-dependent EGF family ligand release by substrate-selecting signaling pathways. Proc. Natl. Acad. Sci. USA 110, 9776–9781. 10.1073/pnas.1307478110. [PubMed: 23720309]
15. Prince RN, Schreiter ER, Zou P, Wiley HS, Ting AY, Lee RT, and Lauffenburger DA (2010). The heparin-binding domain of HB-EGF mediates localization to sites of cell-cell contact and prevents HB-EGF proteolytic release. J. Cell Sci 123, 2308–2318. 10.1242/jcs.058321. [PubMed: 20530570]
16. Gephart JD, Singh B, Higginbotham JN, Franklin JL, Gonzalez A, Fölsch H, and Coffey RJ (2011). Identification of a novel mono-leucine basolateral sorting motif within the cytoplasmic domain of amphiregulin. Traffic 12, 1793–1804. 10.1111/j.1600-0854.2011.01282.x. [PubMed: 21917092]
17. Singh B, Bogatcheva G, Washington MK, and Coffey RJ (2013). Transformation of polarized epithelial cells by apical mistrafficking of epiregulin. Proc. Natl. Acad. Sci. USA 110, 8960–8965. 10.1073/pnas.1305508110. [PubMed: 23671122]
18. Singh B, Bogatcheva G, Starchenko A, Sinnaeve J, Lapierre LA, Williams JA, Goldenring JR, and Coffey RJ (2015). Induction of lateral lumens through disruption of a monoleucine-based basolateral-sorting motif in betacellulin. J. Cell Sci 128, 3444–3455. 10.1242/jcs.170852. [PubMed: 26272915]
19. Inoue H, Sakaue T, Ozawa T, and Higashiyama S (2013). Spatiotemporal visualization of proHB-EGF ectodomain shedding in living cells. J. Biochem 154, 67–76. 10.1093/jb/mvt030. [PubMed: 23598347]
20. Kamezaki A, Sato F, Aoki K, Asakawa K, Kawakami K, Matsuzaki F, and Sehara-Fujisawa A (2016). Visualization of Neuregulin 1 ectodomain shedding reveals its local processing in vitro and in vivo. Sci. Rep 6, 28873. 10.1038/srep28873. [PubMed: 27364328]
21. Bunker EN, Wheeler GE, Chapnick DA, and Liu X (2021). Suppression of α-catenin and adherens junctions enhances epithelial cell prolifertion and motility via TACE-Mediated TGF-α autocrine/paracrine signaling. Mol. Biol. Cell 32, 348–361. 10.1091/mbc.E19-08-0474. [PubMed: 33378218]
22. Hirashima T, Hino N, Aoki K, and Matsuda M (2023). Stretching the limits of extracellular signal-related kinase (ERK) signaling - Cell mechanosensing to ERK activation. Curr. Opin. Cell Biol 84, 102217. 10.1016/j.ceb.2023.102217. [PubMed: 37574635]
23. Aoki K, Kumagai Y, Sakurai A, Komatsu N, Fujita Y, Shionyu C, and Matsuda M (2013). Stochastic ERK activation induced by noise and cell-to-cell propagation regulates cell density-dependent proliferation. Mol. Cell 52, 529–540. 10.1016/j.molcel.2013.09.015. [PubMed: 24140422]
24. Aoki K, Kondo Y, Naoki H, Hiratsuka T, Itoh RE, and Matsuda M (2017). Propagating wave of ERK activation orients collective cell migration. Dev. Cell 43, 305–317.e5. 10.1016/j.devcel.2017.10.016. [PubMed: 29112851]
25. Hiratsuka T, Fujita Y, Naoki H, Aoki K, Kamioka Y, and Matsuda M (2015). Intercellular propagation of extracellular signal-regulated kinase activation revealed by in vivo imaging of mouse skin. Elife 4, e05178. 10.7554/eLife.05178. [PubMed: 25668746]

26. Hino N, Rossetti L, Marín-Llauradó A, Aoki K, Trepat X, Matsuda M, and Hirashima T (2020). ERK-mediated mechanochemical waves direct collective cell polarization. Dev. Cell 53, 646–660.e8. 10.1016/j.devcel.2020.05.011. [PubMed: 32497487]
27. Hino N, Matsuda K, Jikko Y, Maryu G, Sakai K, Imamura R, Tsukiji S, Aoki K, Terai K, Hirashima T, et al. (2022). A feedback loop between lamellipodial extension and HGF-ERK signaling specifies leader cells during collective cell migration. Dev. Cell 57, 2290–2304.e7. 10.1016/j.devcel.2022.09.003. [PubMed: 36174555]
28. Lin S, Hirayama D, Maryu G, Matsuda K, Hino N, Deguchi E, Aoki K, Iwamoto R, Terai K, and Matsuda M (2022). Redundant roles of EGFR ligands in the ERK activation waves during collective cell migration. Life Sci. Alliance 5, e202101206. 10.26508/lsa.202101206. [PubMed: 34667080]
29. Matsuda K, Hirayama D, Hino N, Kuno S, Sakaue-Sawano A, Miyawaki A, Matsuda M, and Terai K (2023). Knockout of all ErbB-family genes delineates their roles in proliferation, survival, and migration. J. Cell Sci 136, 261199. 10.1242/jcs.261199.
30. Ichise H, Tsukamoto S, Hirashima T, Konishi Y, Oki C, Tsukiji S, Iwano S, Miyawaki A, Sumiyama K, Terai K, and Matsuda M (2022). Functional visualization of NK Cell-mediated killing of metastatic single tumor cells. Elife 11, e76269. 10.7554/eLife.76269. [PubMed: 35113018]
31. Le Gall SM, Auger R, Dreux C, and Mauduit P (2003). Regulated cell surface pro-EGF ectodomain shedding is a zinc metalloprotease-dependent process. J. Biol. Chem 278, 45255–45268. 10.1074/jbc.M307745200. [PubMed: 12947092]
32. Kochupurakkal BS, Harari D, Di-Segni A, Maik-Rachline G, Lyass L, Gur G, Kerber G, Citri A, Lavi S, Eilam R, et al. (2005). Epigen, the last ligand of ErbB receptors, reveals intricate relationships between affinity and mitogenicity. J. Biol. Chem 280, 8503–8512. 10.1074/jbc.M413919200. [PubMed: 15611079]
33. Goishi K, Higashiyama S, Klagsbrun M, Nakano N, Umata T, Ishikawa M, Mekada E, and Taniguchi N (1995). Phorbol ester induces the rapid processing of cell surface heparin-binding EGF-like growth factor: conversion from juxtacrine to paracrine growth factor activity. Mol. Biol. Cell 6, 967–980. 10.1091/mbc.6.8.967. [PubMed: 7579712]
34. Suzuki S, Nakamura A, Hatano Y, Yoshikawa M, Yoshii T, Sawada S, Atsuta-Tsunoda K, Aoki K, and Tsukiji S (2022). A chemogenetic platform for controlling plasma membrane signaling and synthetic signal oscillation. Cell Chem. Biol 29, 1446–1464.e10. 10.1016/j.chembiol.2022.06.005. [PubMed: 35835118]
35. Chapnick DA, Bunker E, and Liu X (2015). A biosensor for the activity of the “sheddase” TACE (ADAM17) reveals novel and cell type-specific mechanisms of TACE activation. Sci. Signal. 8, rs1. 10.1126/scisignal.2005680. [PubMed: 25714465]
36. Li C, Franklin JL, Graves-Deal R, Jerome WG, Cao Z, and Coffey RJ (2004). Myristoylated Naked2 escorts transforming growth factor alpha to the basolateral plasma membrane of polarized epithelial cells. Proc. Natl. Acad. Sci. USA 101, 5571–5576. 10.1073/pnas.0401294101. [PubMed: 15064403]
37. Otani T, Nguyen TP, Tokuda S, Sugihara K, Sugawara T, Furuse K, Miura T, Ebnet K, and Furuse M (2019). Claudins and JAM-A coordinately regulate tight junction formation and epithelial polarity. J. Cell Biol 218, 3372–3396. 10.1083/jcb.201812157. [PubMed: 31467165]
38. Singh AB, Tsukada T, Zent R, and Harris RC (2004). Membrane-associated HB-EGF modulates HGF-induced cellular responses in MDCK cells. J. Cell Sci 117, 1365–1379. 10.1242/jcs.01037. [PubMed: 14996914]
39. Ronan T, Macdonald-Obermann JL, Huelsmann L, Bessman NJ, Naegle KM, and Pike LJ (2016). Different Epidermal Growth Factor Receptor (EGFR) Agonists Produce Unique Signatures for the Recruitment of Downstream Signaling Proteins. J. Biol. Chem 291, 5528–5540. 10.1074/jbc.M115.710087. [PubMed: 26786109]
40. Kurokawa K, Mochizuki N, Ohba Y, Mizuno H, Miyawaki A, and Matsuda M (2001). A pair of FRET-based probes for tyrosine phosphorylation of the CrkII adaptor protein in vivo. J. Biol. Chem 276, 31305–31310. 10.1074/jbc.M104341200. [PubMed: 11406630]

41. Li C, Imanishi A, Komatsu N, Terai K, Amano M, Kaibuchi K, and Matsuda M (2017). A FRET biosensor for ROCK based on a consensus substrate sequence identified by KISS technology. Cell Struct. Funct 42, 1–13. 10.1247/csf.16016. [PubMed: 27885213]
42. Brüggemann Y, Karajannis LS, Stanoev A, Stallaert W, and Bastiaens PIH (2021). Growth factor-dependent ErbB vesicular dynamics couple receptor signaling to spatially and functionally distinct Erk pools. Sci. Signal. 14, eabd9943. 10.1126/scisignal.abd9943. [PubMed: 34006609]
43. Shirakata Y, Kimura R, Nanba D, Iwamoto R, Tokumaru S, Morimoto C, Yokota K, Nakamura M, Sayama K, Mekada E, et al. (2005). Heparin-binding EGF-like growth factor accelerates keratinocyte migration and skin wound healing. J. Cell Sci 118, 2363–2370. 10.1242/jcs.02346. [PubMed: 15923649]
44. Shirasawa S, Sugiyama S, Baba I, Inokuchi J, Sekine S, Ogino K, Kawamura Y, Dohi T, Fujimoto M, and Sasazuki T (2004). Dermatitis due to epiregulin deficiency and a critical role of epiregulin in immune-related responses of keratinocyte and macrophage. Proc. Natl. Acad. Sci. USA 101, 13921–13926. 10.1073/pnas.0404217101. [PubMed: 15365177]
45. Komatsu N, Terai K, Imanishi A, Kamioka Y, Sumiyama K, Jin T, Okada Y, Nagai T, and Matsuda M (2018). A platform of BRET-FRET hybrid biosensors for optogenetics, chemical screening, and in vivo imaging. Sci. Rep 8, 8984. 10.1038/s41598-018-27174-x. [PubMed: 29895862]
46. Shvartsman SY, Wiley HS, Deen WM, and Lauffenburger DA (2001). Spatial range of autocrine signaling: modeling and computational analysis. Biophys. J 81, 1854–1867. 10.1016/s0006-3495(01)75837-7. [PubMed: 11566760]
47. DeWitt A, Iida T, Lam H-Y, Hill V, Wiley HS, and Lauffenburger DA (2002). Affinity regulates spatial range of EGF receptor autocrine ligand binding. Dev. Biol 250, 305–316. 10.1006/dbio.2002.0807. [PubMed: 12376105]
48. Reyes NS, Krasilnikov M, Allen NC, Lee JY, Hyams B, Zhou M, Ravishankar S, Cassandras M, Wang C, Khan I, et al. (2022). Sentinel p16(INK4a+) cells in the basement membrane form a reparative niche in the lung. Science 378, 192–201. 10.1126/science.abf3326. [PubMed: 36227993]
49. Neufert C, Becker C, Türeci Ö, Waldner MJ, Backert I, Floh K, Atreya I, Leppkes M, Jefremow A, Vieth M, et al. (2013). Tumor fibroblast-derived epiregulin promotes growth of colitis-associated neoplasms through ERK. J. Clin. Invest 123, 1428–1443. 10.1172/JCI63748. [PubMed: 23549083]
50. Dempsey PJ, and Coffey RJ (1994). Basolateral targeting and efficient consumption of transforming growth factor-alpha when expressed in Madin-Darby canine kidney cells. J. Biol. Chem 269, 16878–16889. 10.1016/S0021-9258(19)89472-3. [PubMed: 8207010]
51. Higashiyama S, Iwamoto R, Goishi K, Raab G, Taniguchi N, Klagsbrun M, and Mekada E (1995). The membrane protein CD9/DRAP 27 potentiates the juxtacrine growth factor activity of the membrane-anchored heparin-binding EGF-like growth factor. J. Cell Biol 128, 929–938. 10.1083/jcb.128.5.929. [PubMed: 7876316]
52. Takemura T, Kondo S, Homma T, Sakai M, and Harris RC (1997). The membrane-bound form of heparin-binding epidermal growth factor-like growth factor promotes survival of cultured renal epithelial cells. J. Biol. Chem 272, 31036–31042. 10.1074/jbc.272.49.31036. [PubMed: 9388253]
53. Li X, Maretzky T, Weskamp G, Monette S, Qing X, Issuree PDA, Crawford HC, McIlwain DR, Mak TW, Salmon JE, and Blobel CP (2015). iRhoms 1 and 2 are essential upstream regulators of ADAM17-dependent EGFR signaling. Proc. Natl. Acad. Sci. USA 112, 6080–6085. 10.1073/pnas.1505649112. [PubMed: 25918388]
54. Tang B, Li X, Maretzky T, Perez-Aguilar JM, McIlwain D, Xie Y, Zheng Y, Mak TW, Weinstein H, and Blobel CP (2020). Substrate-selective protein ectodomain shedding by ADAM17 and iRhom2 depends on their juxtamembrane and transmembrane domains. FASEB J 34, 4956–4969. 10.1096/fj.201902649R. [PubMed: 32103528]
55. Fan H, and Derynck R (1999). Ectodomain shedding of TGF-alpha and other transmembrane proteins is induced by receptor tyrosine kinase activation and MAP kinase signaling cascades. EMBO J 18, 6962–6972. 10.1093/emboj/18.24.6962. [PubMed: 10601018]
56. Miller MA, Meyer AS, Beste MT, Lasisi Z, Reddy S, Jeng KW, Chen CH, Han J, Isaacson K, Griffith LG, and Lauffenburger DA (2013). ADAM-10 and −17 regulate endometriotic cell migration via concerted ligand and receptor shedding feedback on kinase signaling. Proc. Natl. Acad. Sci. USA 110, E2074–E2083. 10.1073/pnas.1222387110. [PubMed: 23674691]

57. Gagliardi PA, Dobrzyński M, Jacques M-A, Dessauges C, Ender P, Blum Y, Hughes RM, Cohen AR, and Pertz O (2021). Collective ERK/Akt activity waves orchestrate epithelial homeostasis by driving apoptosis-induced survival. Dev. Cell 56, 1712–1726.e1716. 10.1016/j.devcel.2021.05.007. [PubMed: 34081908]
58. Valon L, Davidović A, Levillayer F, Villars A, Chouly M, Cerqueira-Campos F, and Levayer R (2021). Robustness of epithelial sealing is an emerging property of local ERK feedback driven by cell elimination. Dev. Cell 56, 1700–1711.e1708. 10.1016/j.devcel.2021.05.006. [PubMed: 34081909]
59. Nakamura A, Oki C, Sawada S, Yoshii T, Kuwata K, Rudd AK, Devaraj NK, Noma K, and Tsukiji S (2020). Designer Palmitoylation Motif-Based Self-Localizing Ligand for Sustained Control of Protein Localization in Living Cells and Caenorhabditis elegans. ACS Chem. Biol 15, 837–843. 10.1021/acschembio.0c00014. [PubMed: 32182034]
60. Bindels DS, Haarbosch L, van Weeren L, Postma M, Wiese KE, Mastop M, Aumonier S, Gotthard G, Royant A, Hink MA, and Gadella TWJ Jr. (2017). mScarlet: a bright monomeric red fluorescent protein for cellular imaging. Nat. Methods 14, 53–56. 10.1038/nmeth.4074. [PubMed: 27869816]
61. Yusa K, Rad R, Takeda J, and Bradley A (2009). Generation of transgene-free induced pluripotent mouse stem cells by the piggyBac transposon. Nat. Methods 6, 363–369. 10.1038/nmeth.1323. [PubMed: 19337237]
62. Kawabata N, and Matsuda M (2016). Cell density-dependent increase in tyrosine-monophosphorylated ERK2 in MDCK cells expressing active Ras or Raf. PLoS One 11, e0167940. 10.1371/journal.pone.0167940. [PubMed: 27936234]
63. Schindelin J, Arganda-Carreras I, Frise E, Kaynig V, Longair M, Pietzsch T, Preibisch S, Rueden C, Saalfeld S, Schmid B, et al. (2012). Fiji: an open-source platform for biological-image analysis. Nat. Methods 9, 676–682. 10.1038/nmeth.2019. [PubMed: 22743772]
64. Sunagawa GA, Sumiyama K, Ukai-Tadenuma M, Perrin D, Fujishima H, Ukai H, Nishimura O, Shi S, Ohno R. i., Narumi R, et al. (2016). Mammalian reverse genetics without crossing reveals Nr3a as a short-sleeper gene. Cell Rep 14, 662–677. 10.1016/j.cel-rep.2015.12.052. [PubMed: 26774482]
65. Shaner NC, Lambert GG, Chammas A, Ni Y, Cranfill PJ, Baird MA, Sell BR, Allen JR, Day RN, Israelsson M, et al. (2013). A bright monomeric green fluorescent protein derived from Branchiostoma lanceolatum. Nat. Methods 10, 407–409. 10.1038/nmeth.2413. [PubMed: 23524392]
66. Briley GP, Hissong MA, Chiu ML, and Lee DC (1997). The carboxyl-terminal valine residues of proTGF alpha are required for its efficient maturation and intracellular routing. Mol. Biol. Cell 8, 1619–1631. 10.1091/mbc.8.8.1619. [PubMed: 9285829]
67. Dempsey PJ, Meise KS, and Coffey RJ (2003). Basolateral sorting of transforming growth factor-a precursor in polarized epithelial cells: characterization of cytoplasmic domain determinants. Exp. Cell Res 285, 159–174. 10.1016/s0014-4827(03)00035-1. [PubMed: 12706112]
68. Miyoshi H, Verma IM, Blömer U, Takahashi M, and Gage FH (1998). Development of a Self-Inactivating Lentivirus Vector. J. Virol 72, 8150–8157. 10.1128/JVI.72.10.8150-8157.1998. [PubMed: 9733856]
69. Naito Y, Hino K, Bono H, and Ui-Tei K (2015). CRISPRdirect: software for designing CRISPR/Cas guide RNA with reduced off-target sites. Bioinformatics 31, 1120–1123. 10.1093/bioinformatics/btu743. [PubMed: 25414360]
70. Sanjana NE, Shalem O, and Zhang F (2014). Improved vectors and genome-wide libraries for CRISPR screening. Nat. Methods 11, 783–784. 10.1038/nmeth.3047. [PubMed: 25075903]
71. Ran FA, Hsu PD, Wright J, Agarwala V, Scott DA, and Zhang F (2013). Genome engineering using the CRISPR-Cas9 system. Nat. Protoc 8, 2281–2308. 10.1038/nprot.2013.143. [PubMed: 24157548]
72. Aoki K, and Matsuda M (2009). Visualization of small GTPase activity with fluorescence resonance energy transfer-based biosensors. Nat. Protoc 4, 1623–1631. 10.1038/nprot.2009.175. [PubMed: 19834477]

73. Tinevez J-Y, Perry N, Schindelin J, Hoopes GM, Reynolds GD, Laplantine E, Bednarek SY, Shorte SL, and Eliceiri KW (2017). TrackMate: An open and extensible platform for single-particle tracking. Methods 115, 80–90. 10.1016/j.ymeth.2016.09.016. [PubMed: 27713081]

74. Tsujino K, Narumi R, Masumoto KH, Susaki EA, Shinohara Y, Abe T, Iigo M, Wada A, Nagano M, Shigeyoshi Y, and Ueda HR (2013). Establishment of TSH b real-time monitoring system in mammalian photoperiodism. Gene Cell. 18, 575–588. 10.1111/gtc.12063.

75. Watabe T, Yamahira S, Takakura K, Thumkeo D, Narumiya S, Matsuda M, and Terai K (2023). Calcium transients trigger switch-like discharge of prostaglandin E2 (PGE2) in an ERK-dependent manner. Elife 12, RP86727. 10.7554/elife.86727.1.

Highlights

- EGFRL probes visualize the dynamics of individual EGFRLs in the extracellular space
- Chemogenetic EGFRL shedding induces ERK activation in surrounding cells
- Low-affinity EGFRLs diffuse farther compared to high-affinity ones
- EREG plays a role in collective cell migration and skin wound repair *in vivo*

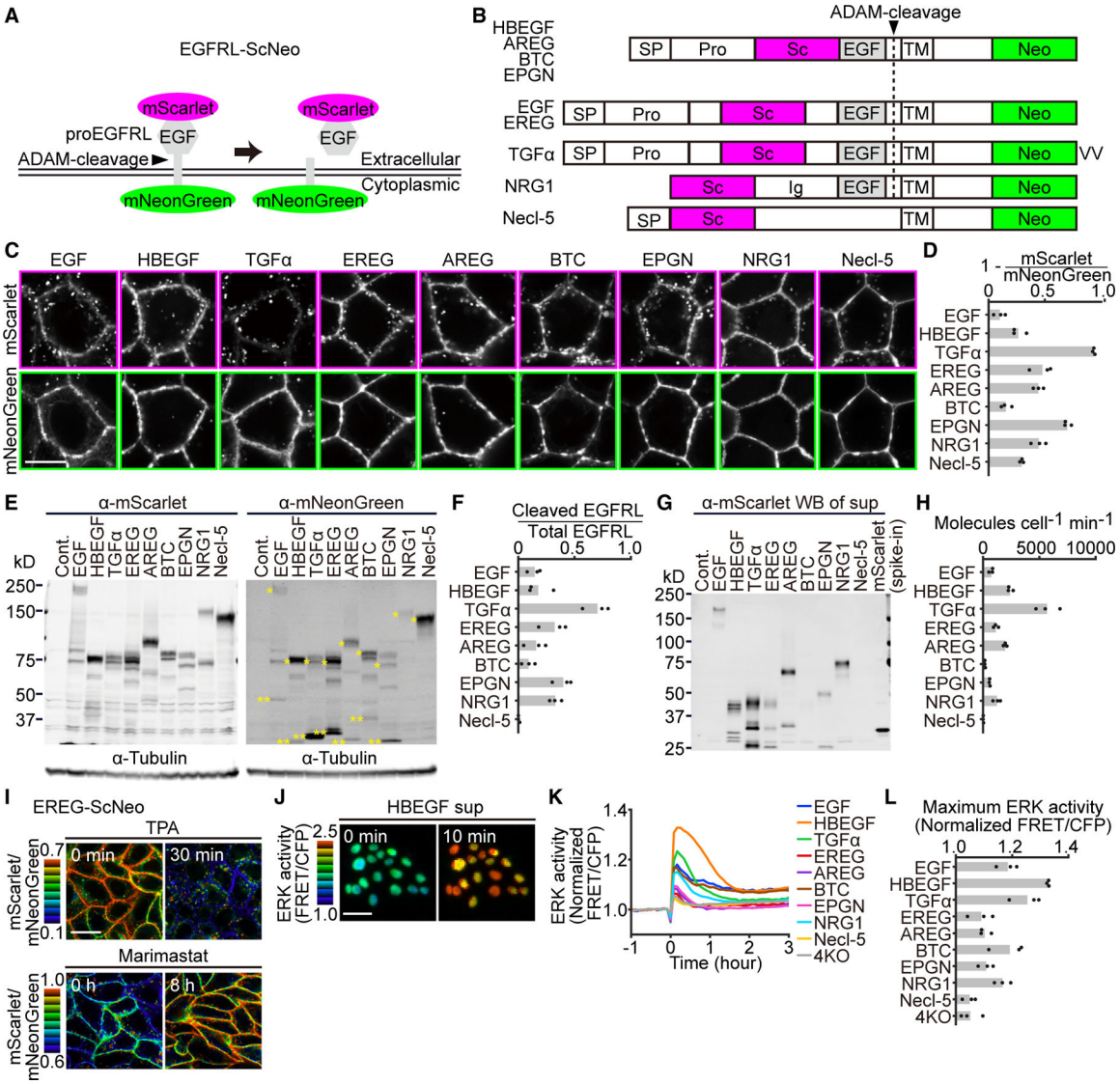

Figure 1. EGFRL-ScNeos visualize the shedding of EGFRLs and stimulate EGFR

(A) Schematic of EGFRL-ScNeo expressed at the cell membrane.

(B) Structure of EGFRL-ScNeos. SP, signal peptide; Pro, propeptide; Sc, mScarlet; EGF, EGF domain; TM, transmembrane domain; Neo, mNeonGreen; VV, two valine residues; Ig, immunoglobulin-like domain.

(C) xy confocal images of EGFRL-ScNeos. Scale bar, 10 μm.

(D) mScarlet/mNeonGreen fluorescence ratio of the cell membrane. The bar graphs show the mean values. Each dot represents the average value for one experiment (n > 100 cells/ experiment).

(E) Western blot analysis of total cell lysates of EGFRL-ScNeo-expressing cells. *Full-length EGFRL-ScNeo; **cytoplasmic domain with mNeonGreen.

(F) The proportion of cleaved EGFRL-ScNeo in (E). The bar graphs show the mean values. Each dot indicates an independent experiment.

(G) Western blot analysis of supernatants of EGFRL-ScNeo-expressing cells.

(H) The production rates of EGFRL from a single EGFRL-ScNeo-expressing cell. The bar graphs show the mean values. Each dot indicates an independent experiment.
(I) mScarlet/mNeonGreen ratio images of EREG-ScNeo-expressing MDCK cells upon treatment with 10 nM TPA or 10 μM marimastat (Video S1). Scale bar, 20 μm.
(J) ERK activity of MDCK-4KO cells expressing EKARrEV-NLS stimulated with the supernatant of MDCK-4KO cells expressing HBEGF-ScNeo. Scale bar, 50 μm.
(K) Time course of ERK activity in MDCK-4KO-EKARrEV-NLS cells stimulated with supernatant from MDCK-4KO cells expressing EGFRL-ScNeo. Solid lines represent the means from two independent experiments (n > 1,000 cells/experiment).
(L) Maximum ERK activity from the time course shown in (K). The bar graphs show the mean values from three independent experiments. Each dot represents the average value for one experiment (n > 1,000 cells/experiment). See also Figure S1 and Video S1.

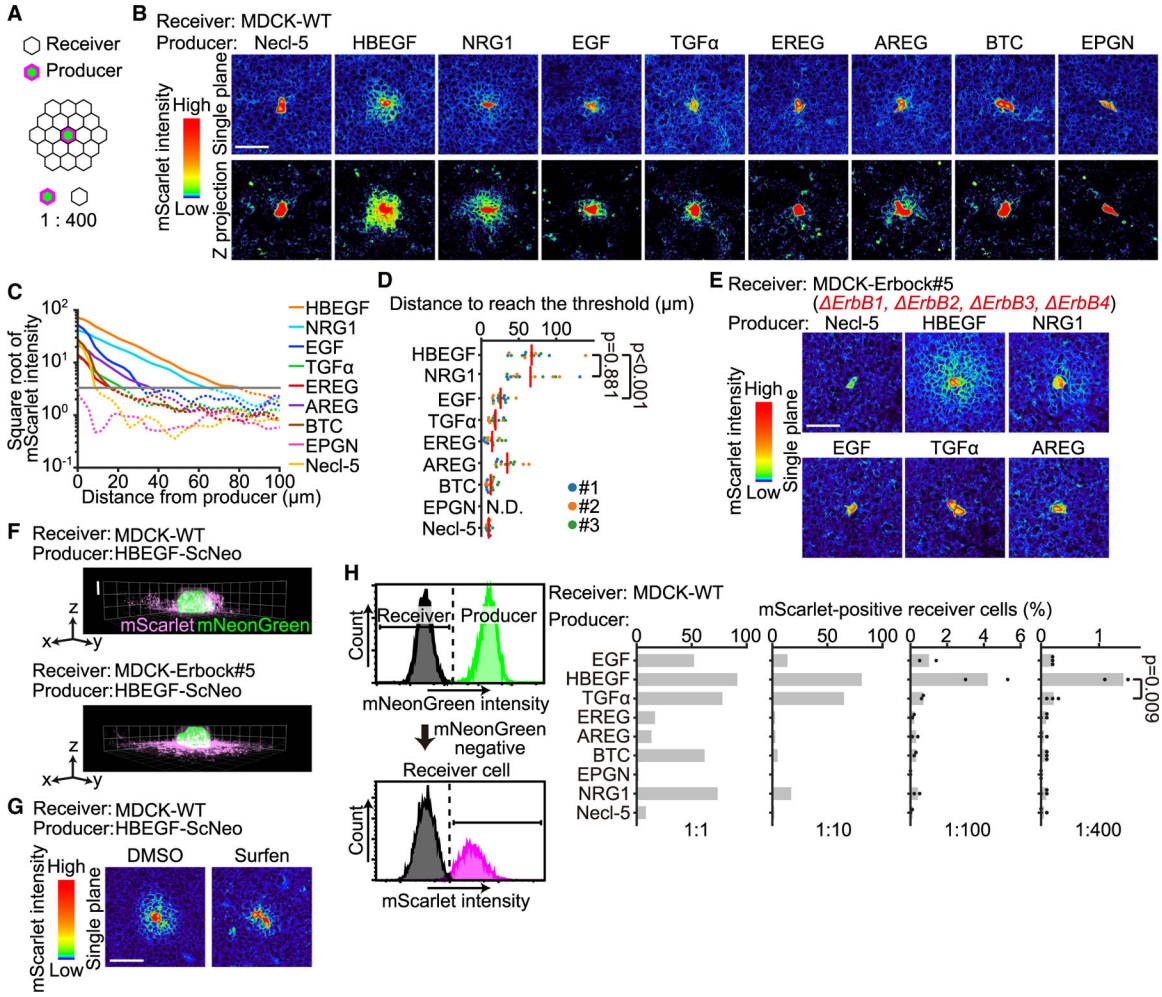

Figure 2. EGFRL-ScNeo highlights short- and long-range EGFRLs

(A) Schematic of the co-culture experiment. Producer, EGFRL-ScNeo-expressing MDCK cells; receiver, parental MDCK cells. Producer and receiver cells were co-cultured at a 1:400 ratio.

(B) Representative mScarlet confocal images of a single plane and z projection (20 slices) for each EGFRL, with producer cells identified by central signals above a threshold. Scale bar, 100 μm.

(C) mScarlet signal gradient from producer cells in (B). Solid lines represent the means from three independent experiments, five images each. The gray bar indicates the threshold of detectable mScarlet signals.

(D) Distance from producer cells to reach the threshold indicated in (C) is represented as dots. The red bars represent the means from three independent experiments, depicted by the three colors (n = 5 images/experiment). p values were calculated by a two-sample unpaired t test.

(E) Identical to (B) except that the receiver cells were MDCK-Erbock cells, lacking all four ErbB-family receptors. Scale bar, 100 μm.

(F) Three-dimensional images of HBEGF-ScNeo cells co-cultured with WT or MDCK-Erbock cells. Scale bar, 10 μm.

(G) mScarlet confocal images of receiver and producer cells co-cultured with 0.1% DMSO or 5 μM surfen. Scale bar, 100 μm.

(H) (Left) Schematic of flow cytometry analysis of co-culture experiments. (Right) The proportion of mScarlet-positive receiver-cells at different producer versus receiver ratios. The bar graphs show the mean values (n = 1 for 1:1 and 1:10, n = 2 for 1:100, n = 3 for 1:400). Each dot represents an independent experiment. p value was calculated by a two-sample unpaired t test. See also Figure S2.

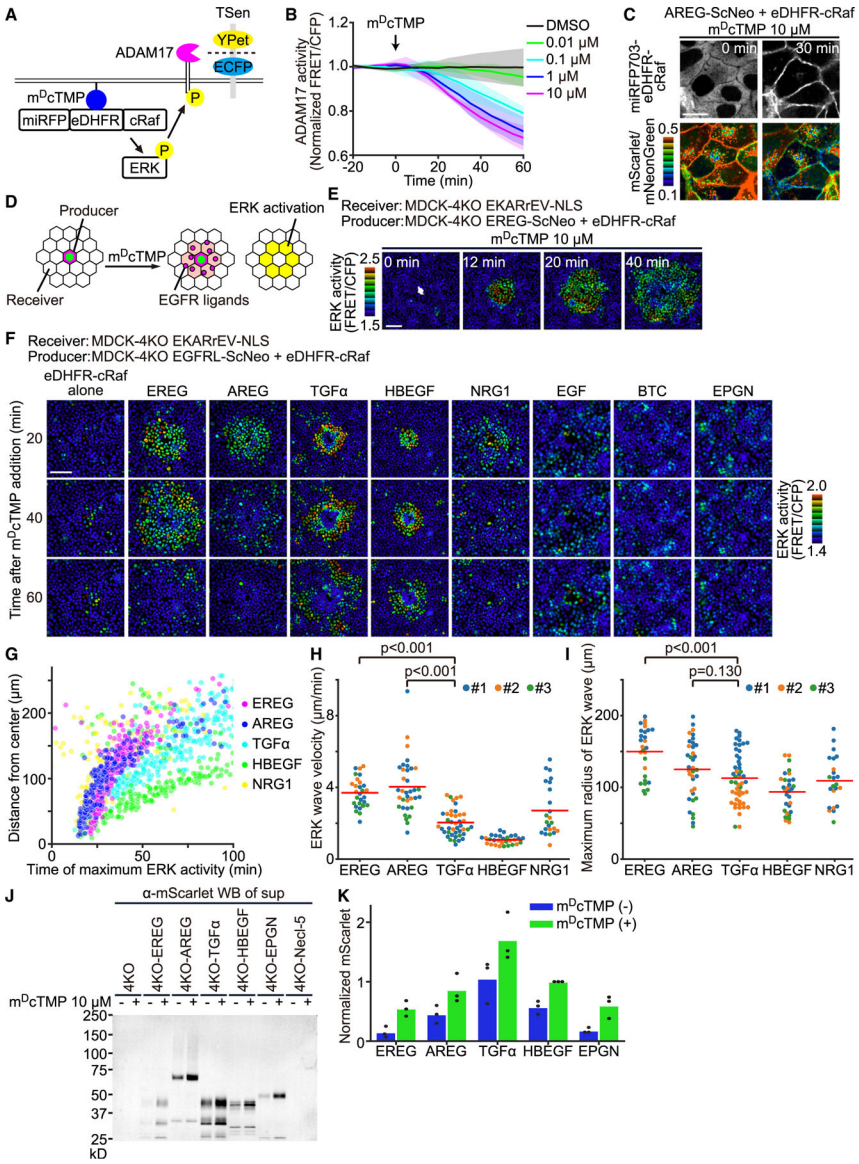

Figure 3. Low-affinity EGFRLs propagate ERK activation more efficiently than high-affinity EGFRLs

(A) Schematic of the SLIPT system.

(B) Time course of normalized FRET/CFP ratio for TSen stimulated with various m^{D}cTMP concentrations. Values were normalized to the average pre-stimulation baseline (20 min). Solid lines and shaded areas represent means and SDs from three independent experiments (n > 100 cells/experiment).

(C) miRFP703 and mScarlet/mNeonGreen ratio images of cells expressing AREG-ScNeo and eDHFR-cRaf. Images are snapshots of Video S2. Scale bar, 20 μm.

(D) Schematic of SLIPT-induced EGFRL shedding and ERK activity observation.

(E) Representative time-lapse ERK activity images. The white area at the center of the 0 min image indicates the EREG-producer cells. Scale bar, 100 μm.

(F) Representative time-lapse ERK activity images. Each ligand producer is located at the center of the image. Images are snapshots of Video S3. Scale bar, 100 μm.

(G) The time of maximum ERK activity in receiver cells in (F) after m^{D}cTMP addition is plotted against the distance from the center. Each dot indicates a single cell.
(H) Velocities of ERK waves propagated from each EGFRL producer. Each dot indicates a single producer-cell population. The red bars represent the means from three independent experiments, depicted by the three colors (n = 28 [EREG], 36 [AREG], 50 [TGF-α], 30 [HBEGF], and 23 [NRG1] producer-cell populations). p values were calculated by a two-sample unpaired t test.
(I) Maximum radius of ERK waves propagated from each EGFRL producer. Data in (H) were used for the analysis. The red bars represent the means. p values were calculated by a two-sample unpaired t test.
(J) Western blot analysis of the supernatant of each producer cell incubated with or without 10 μM m^{D}cTMP.
(K) The production rates of EGFRL from each producer cell in (J). The mScarlet intensities of HBEGF supernatant with m^{D}cTMP were set as 1. See also Figures S3 and S4 and Videos S2 and S3.

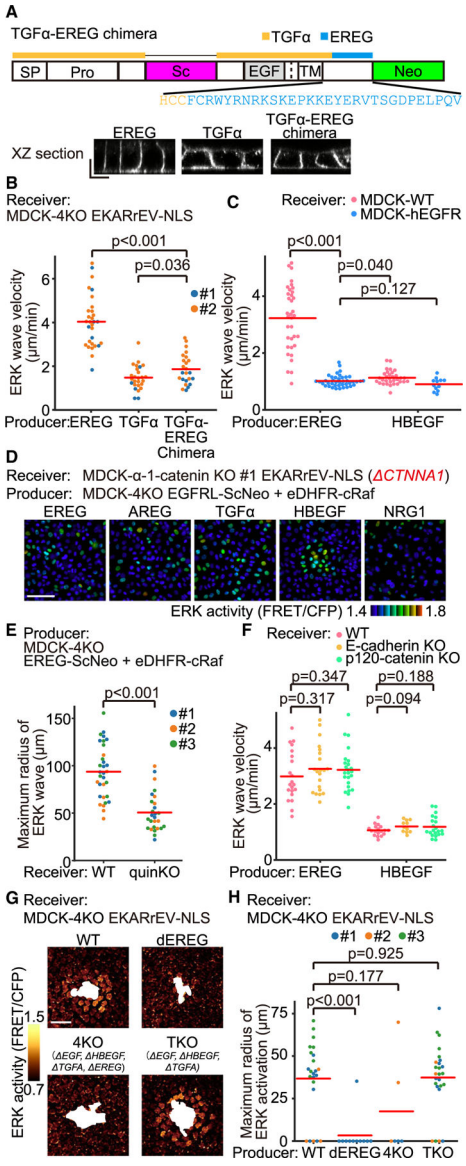

Figure 4. Diffusion of EGFRL in the intercellular space is regulated by the affinity to and the density of EGFR on the basolateral plasma membrane

(A) (Top) Schematic of TGF-α-EREG chimera. (Bottom) mNeonGreen xz images of EREG, TGF-α, and a TGF-α-EREG chimera. Scale bars, 10 μm.

(B) The velocity of the ERK wave propagated from each producer. Each dot indicates a single producer-cell population. The red bars represent the means from two independent experiments, depicted by the two colors (n = 30 [EREG], 26 [TGF-α], and 24 [TGF-α-EREG chimera] producer-cell populations). p values were calculated by a two-sample unpaired t test.

(C) The velocity of the ERK wave propagated from each producer cell to WT or EGFR-overexpressing (O/E) receiver cells. Each dot indicates a single producer-cell population. The red bars represent the means from two independent experiments (n = 35 [EREG, WT], 41 [EREG, EGFR O/E], 32 [HBEGF, WT], and 12 [HBEGF, EGFR O/E] producer-cell populations). p values were calculated by a two-sample unpaired t test.

(D) Representative ERK activity images in MDCK-α−1-catenin KO receiver cells. Each EGFRL producer cell is located at the center. Images were acquired 30 min after m^{D}cTMP addition (Video S4). Scale bar, 100 μm.

(E) Maximum radius of the ERK wave propagated from each EREG-producer cell to each receiver cell. Each dot indicates a single producer-cell population. The red bars represent the means from three independent experiments, depicted by the three colors (n = 38 [WT] and 42 [quinKO] producer-cell populations). p values were calculated by a two-sample unpaired t test.

(F) The velocity of the ERK wave propagated from each producer cell to each receiver cell. Each dot indicates a single producer-cell population. The red bars represent the means from two independent experiments (n = 21 [EREG, WT], 21 [EREG, E-cadherin KO], 24 [EREG, p120-catenin KO], 18 [HBEGF, WT], 11 [HBEGF, E-cadherin KO], and 21 [HBEGF, p120-catenin KO] producer-cell populations). p values were calculated by two-sample unpaired t test.

(G) Representative ERK activity images in MDCK-4KO-EKARrEV-NLS receiver cells. Each producer cell expressing eDHFR-cRaf is located in the white area. Images were acquired 20 min after m^{D}cTMP addition. Scale bar, 50 μm.

(H) Maximum radius of the ERK wave propagation in (G). Each dot indicates a single producer-cell population. The red bars represent the means. n = 23 (WT) or 25 (TKO) producer-cell populations from three independent experiments. n = 6 (4KO) producer-cell populations from two independent experiments. n = 11 (dEREG) producer-cell populations from a single experiment. p values were calculated by a two-sample unpaired t test. See also Figure S5 and Video S4.

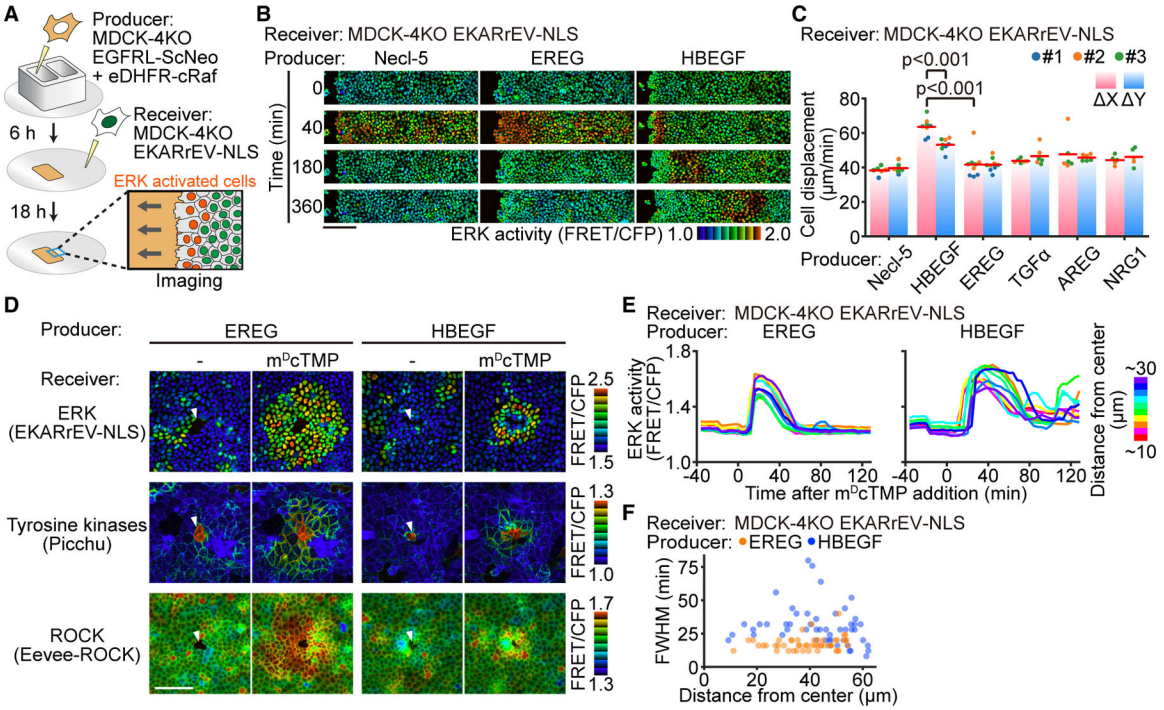

Figure 5. HBEGF but not EREG promotes collective cell migration

(A) Schematic of the boundary assay.

(B) Representative ERK activity images in receiver cells adjacent to each producer cell (Video S5). m^{D}cTMP was added at 0 min. Scale bar, 100 μm.

(C) Receiver-cell displacement adjacent to each producer cell. The red lines show the mean values. Each dot represents the average of a single field of view. n > 1,000 cells from three independent experiments, depicted by the three colors. p values were calculated by a two-sample unpaired t test.

(D) Representative FRET/CFP images of receiver cells expressing ERK, tyrosine kinases, or ROCK biosensors. White arrowheads indicate the location of EGFRL-producer cells. Images were acquired 32 min after m^{D}cTMP addition (Video S6). Scale bar, 100 μm.

(E) ERK activity in 10 representative cells around EREG or HBEGF producers was plotted over time after m^{D}cTMP addition.

(F) FWHM of ERK activation in receiver cells. Each dot indicates a single receiver cell. n = 50 cells from a single experiment. See also Videos S5 and S6.

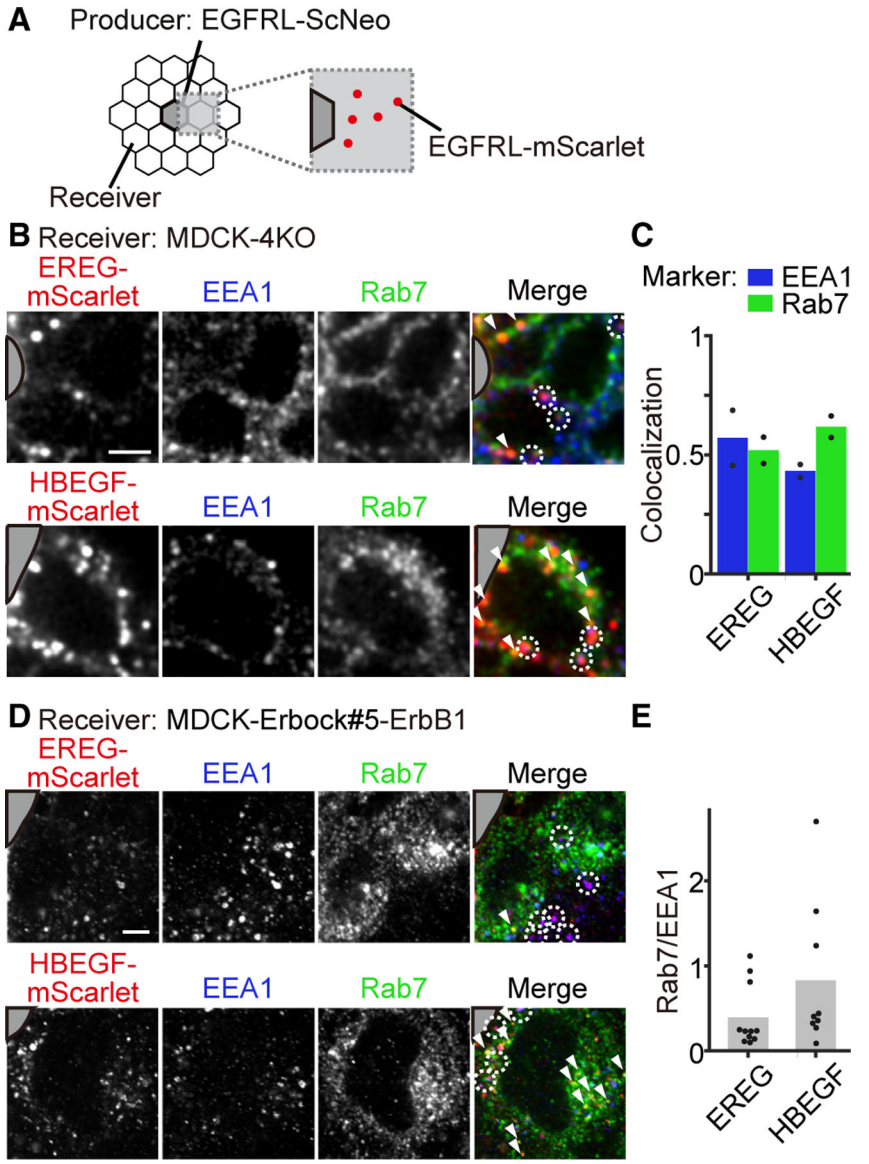

Figure 6. HBEGF but not EREG is sorted to late endosomes

(A) Schematic of the experiment.

(B) MDCK-4KO receiver cells surrounding EREG-ScNeo or HBEGF-ScNeo producer-cells. Cells were fixed and stained with anti-EEA1 and anti-Rab7 antibodies. White circles and arrowheads indicate mScarlet-positive vesicles co-localized with EEA1 and Rab7, respectively. The gray area indicates the producer cells. Scale bar, 5 μm.

(C) Fraction of mScarlet-positive vesicles co-localized with EEA1 or Rab7 from images in (B). The bar graphs show the mean values. Each dot represents the average of a single field of view. $n = 2$ fields of view from a single experiment.

(D) MDCK-Erbock-ErbB1 receiver cells surrounding EREG-ScNeo or HBEGF-ScNeo producer cells. Cells were fixed and stained with anti-EEA1, anti-Rab7, and anti-RFP antibody. Scale bar, 5 μm.

(E) The proportion of mScarlet-positive vesicles co-localized with Rab7 or EEA1 from experiments in (D). The bar graphs show the mean values. Each dot represents the average of a single field of view. $n = 11$ (EREG) or 9 (HBEGF) fields of view from three independent experiments.

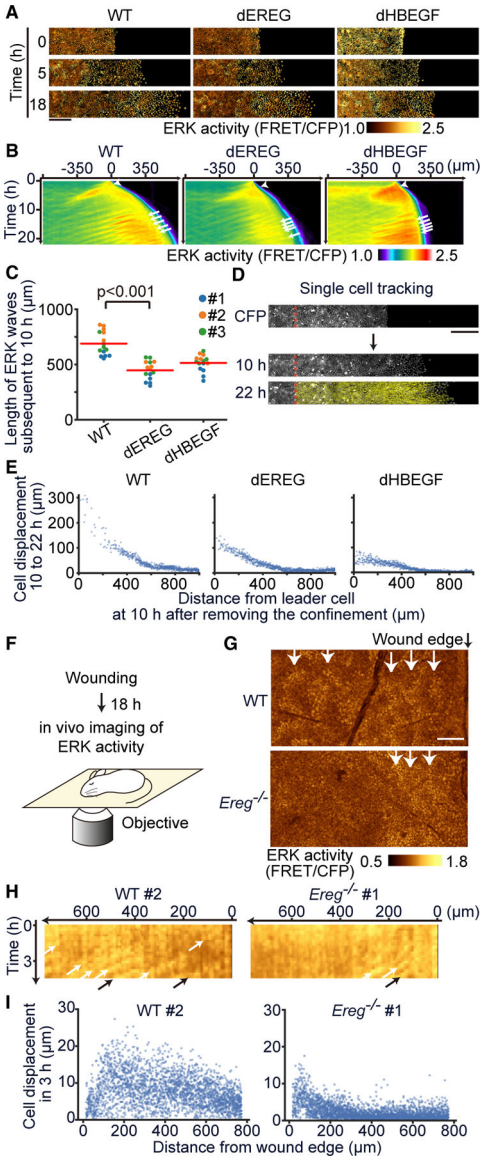

Figure 7. EREG is required for collective cell migration of wounded mouse epidermis

(A) ERK activity images in migrating MDCK WT, dEREG, or dHBEGF cells. Scale bar, 200 μm.

(B) Kymographs of ERK activity generated from time-lapse FRET/CFP ratio images. White arrowheads indicate the first ERK wave propagating from the leader cells. White arrows indicate ERK waves propagating from the leader cells 10 h after removing the confinement.

(C) Length of ERK waves propagating from the leader cells 10 h after removing the confinement. Each dot indicates a single ERK wave. Each color represents data from a single experiment. The red bars represent the means. p value was calculated by a two-sample unpaired t test.

(D) Representative images of single-cell trajectories 10 to 22 h after removing the confinement. Scale bar, 200 μm.

(E) Displacement of MDCK cells at 10 to 22 h after removing the confinement. Each dot represents a single cell. $n > 1{,}000$ cells for each experiment.
(F) Schematic of an *in vivo* imaging of ERK activity during wound healing of mouse ear skin expressing hyBRET-ERK-NLS.
(G) Representative ERK activity images in WT or *Ereg*$^{-/-}$ mouse ear skin (Video S7). White arrows indicate ERK waves propagating from the wound edge (right black arrow). Scale bar, 100 μm.
(H) Kymographs of ERK activity generated from time-lapse FRET/CFP ratio images. White and black arrows indicate ERK waves propagating from the wound edge (0 μm).
(I) Displacement of mouse skin basal layer cells in 3 h toward the wound edge. Each dot represents a single cell. $n > 1{,}000$ cells for each mouse. See also Figure S6 and Video S7.

KEY RESOURCES TABLE

REAGENT or RESOURCE	SOURCE	IDENTIFIER
Antibodies		
Anti-mCherry rabbit antibody	abcam	Cat# ab167453; RRID: AB_2571870
Anti-mNeonGreen rabbit antibody	Cell Signaling Technology	Cat# 53061; RRID: AB_2799426
anti-phospho-EGFR (Tyr1068) rabbit antibody	Cell Signaling Technology	Cat# 3777; RRID: AB_2096270
Anti-alpha Tubulin mouse antibody (DM1A)	Thermo Fisher Scientific	Cat# 62204; RRID: AB_1965960
IRDye 680-conjugated goat anti-mouse IgG antibody	LI-COR Biosciences	Cat# 926-32220; RRID: AB_621840
IRDye 800CW goat anti-rabbit IgG antibody	LI-COR Biosciences	Cat# 926-32211; RRID: AB_621843
anti-GP135 mouse antibody	Merck Millipore	Cat# MABS1327; RRID: AB_3102002
anti-ZO-1 rabbit antibody	Thermo Fisher Scientific	Cat# 40-2200; RRID: AB_2533456
anti-EEA1 mouse antibody	BD Biosciences	Cat# 610457; RRID: AB_397830
anti-Rab7 rabbit antibody	Cell Signaling Technology	Cat#9367; RRID: AB_1904103
Anti-RFP rat antibody	Chromo tek	Cat#5f8; RRID: AB_2336064
AMCA-conjugated donkey anti-mouse IgG (H+L) antibody	Jackson ImmunoResearch	Cat#715-155-151; RRID: AB_2340807
Cy5-conjugated donkey anti-rabbit IgG (H+L) antibody	Jackson ImmunoResearch	Cat#711-175-152; RRID: AB_2340607
Alexa 405-conjugated goat anti-mouse IgG (H+L) antibody	Thermo Fisher Scientific	Cat# A-31553; RRID: AB_221604
Alexa 546-conjugated goat anti-rat IgG (H+L) antibody	Thermo Fisher Scientific	Cat# A-11081; RRID: AB_2534125
Alexa 647-conjugated goat anti-rabbit IgG (H+L) antibody	Thermo Fisher Scientific	Cat# A-21245; RRID: AB_2535813
Bacterial and virus strains		
ArcticExpress (DE3) Competent Cells	Agilent Technologies	Cat# 230192
Chemicals, peptides, and recombinant proteins		
DMEM	Wako	Cat# 044-29765
FBS	Sigma-Aldrich	Cat# F7524
Penicillin-Streptomycin	Nacalai Tesque	Cat# 26253-84
Medium 199	Life Technologies	Cat# 11043023
Cellmatrix Type I -C (Collagen, Type I, 3 mg mL^{-1}, pH 3.0)	Nitta Gelatin	Cat# 637-00773
Dimethyl sulfoxide	Nacalai Tescue	Cat# 13445-74; CAS: 67-68-5
12-O-tetradecanoylphorbol 13-acetate (TPA)	LC Laboratories	Cat# P-1680; CAS: 16561-29-8
Marimastat	Santa Cruz Biotechnology	Cat# SC-202223; CAS:154039-60-8
Trametinib	LC Laboratories	Cat# T-8123; CAS:871700-17-3
Surfen	Sigma-Aldrich	Cat# S6951; CAS: 5424-37-3
Cytochalasin D	Calbiochem	Cat# 250255; CAS:22144-77-0
Recombinant human EGF	Sigma-Aldrich	Cat# E9644; CAS: 62253-63-8
Recombinant human HB-EGF	PeproTech	Cat# 100-47
Recombinant human EREG	PeproTech	Cat# 100-04
Recombinant human TGFα	R&D Systems	Cat# 239-A-100

REAGENT or RESOURCE	SOURCE	IDENTIFIER
Bovine serum albumin	Sigma-Aldrich	Cat# A2153
m^{D}cTMP	Nakamura et al.[59]	N/A
Polyethyleneimine	Polyscience Inc.	Cat# 24765-1
Puromycin dihydrochloride	Sigma-Aldrich	Cat# P-8833; CAS: 58-58-2
Blasticidin S Hydrochloride	Wako	Cat# 029-18701; CAS: 3513-03-9
Zeocin	Thermo Fisher Scientific	Cat# R25005; CAS: 11006-33-0
Deposited data		
Microscopy data	Systems Science of Biological Dynamics repository (SSBD:repository)	https://doi.org/10.24631/ssbd.repos.2024.03.342
Experimental models: Cell lines		
Dog: MDCK cells	RIKEN BioResource Center	RCB0995
Human: Lenti-X 293T cells	Clontech	632180
Dog: MDCK-EKARrEV-NLS	Japanese Collection of Research Bioresources (JCRB) Cell Bank	JCRB1973
Dog: MDCK-EKARrEV-NLS-dEGFR	Japanese Collection of Research Bioresources (JCRB) Cell Bank	JCRB1994
Dog: MDCK-4KO	Japanese Collection of Research Bioresources (JCRB) Cell Bank	JCRB1967
Dog: MDCK-4KO-EKARrEV-NLS	Japanese Collection of Research Bioresources (JCRB) Cell Bank	JCRB1990
Dog: MDCK-TKO-EKARrEV-NLS	Japanese Collection of Research Bioresources (JCRB) Cell Bank	JCRB1983
Dog: MDCK-EKARrEV-NLS-dEREG	Japanese Collection of Research Bioresources (JCRB) Cell Bank	JCRB1980
Dog: MDCK-dHBEGF-EKARrEV-NLS	Japanese Collection of Research Bioresources (JCRB) Cell Bank	JCRB1975
Dog: MDCK-Erbock#5	Japanese Collection of Research Bioresources (JCRB) Cell Bank	N/A
Dog: MDCK-EKARrEV-NLS-dErbB1-dErbB3-dErbB4#1	Japanese Collection of Research Bioresources (JCRB) Cell Bank	N/A
Dog: MDCK II	Otani et al.[37]	N/A
Dog: quinKO	Otani et al.[37]	N/A
Experimental models: Organisms/strains		
Mouse: hyBRET-ERK-NLS	Laboratory Animal Resource Bank at NIBIOHN, Japan	nbio326
Mouse: hyBRET-ERK-NLS Ereg−/−	Laboratory Animal Resource Bank at NIBIOHN, Japan	nbio448
Oligonucleotides		
sgRNA targeting sequence: E-cadherin: CGGGGGCGCCGCCGTACCGA	This paper	N/A
sgRNA targeting sequence: p120-catenin: GGGCGTGACTTCCGCAAGAA	This paper	N/A
crRNA targeting sequence: Ereg #1: GCGTCAAGACCCAAGAGGCA	This paper	N/A
crRNA targeting sequence: Ereg #2: CGTATTCTTTGCTCAAGGGT	This paper	N/A

REAGENT or RESOURCE	SOURCE	IDENTIFIER
Primers for validating *Ereg* knockout by qPCR, see Table S1	This paper	N/A
Recombinant DNA		
pmScarlet_C1	Bindels et al.[60]	Addgene plasmid #85042
pro-EGF	Biological Resource Center, National Institute of Technology and Evaluation	Acc #AK299306
pro-HBEGF	a gift from Ryo Iwamoto (Osaka University, Japan)	N/A
pro-TGFα	a gift from Ryo Iwamoto (Osaka University, Japan)	N/A
pCMV-VSVG-RSV-Rev	a gift from Hiroyuki Miyoshi (RIKEN BioResource Center, Japan)	N/A
psPAX2	a gift from Didier Trono (Ecole Polytechnique Fé dérale de Lausanne, Switzerland)	Addgene plasmid #12260
pCMV-mPBase(neo-)	Yusa et al.[61]	N/A
pCSIIpuro-EGF-ScNeo	This paper	Addgene plasmid #209893
pCSIIpuro-HBEGF-ScNeo	This paper	Addgene plasmid #209894
pCSIIpuro-TGFa-ScNeo	This paper	Addgene plasmid #209895
pCSIIpuro-EREG-ScNeo	This paper	Addgene plasmid #209896
pCSIIpuro-AREG-ScNeo	This paper	Addgene plasmid #209897
pCSIIpuro-BTC-ScNeo	This paper	Addgene plasmid #209898
pCSIIpuro-EPGN-ScNeo	This paper	Addgene plasmid #209899
pCSIIpuro-NRG1-ScNeo	This paper	Addgene plasmid #209900
pCSIIpuro-Necl5-ScNeo	This paper	Addgene plasmid #209901
pPBbleo-EGF-ScNeo	This paper	Addgene plasmid #209902
pPBbleo-HBEGF-ScNeo	This paper	Addgene plasmid #209903
pPBbleo-TGFa-ScNeo	This paper	Addgene plasmid #209904
pPBbleo-EREG-ScNeo	This paper	Addgene plasmid #209905
pPBpuro-NRG1-ScNeo	This paper	Addgene plasmid #209906
pPBbsr2-HBEGF-ScNeo	This paper	Addgene plasmid #209907
pPBbsr2-TGFa-ScNeo	This paper	Addgene plasmid #209908
pPBbsr2-EREG-ScNeo	This paper	Addgene plasmid #209909
pPBbsr2-AREG-ScNeo	This paper	Addgene plasmid #209910
pPBbsr2-NRG1-ScNeo	This paper	Addgene plasmid #209911
pCSIIpuro-HBEGF-mNeonGreen	This paper	Addgene plasmid #209912
pCSIIpuro-TGFa-mNeonGreen	This paper	Addgene plasmid #209913
pCSIIpuro-EREG-mNeonGreen	This paper	Addgene plasmid #209914
pPBbleo-TGFa-EREG-ScNeo	This paper	Addgene plasmid #209915
pPBpuro-ErbB1	Matsuda et al.[29]	Addgene plasmid #197358
pPBbleo-ErbB1	Matsuda et al.[29]	Addgene plasmid #197359
pCSIIbsr-EKARrEV-NLS	Lin et al.[28]	Addgene plasmid # 173854

REAGENT or RESOURCE	SOURCE	IDENTIFIER
pPBbsr2-EKARrEV-NLS	Lin et al.[28]	Addgene plasmid #173855
pT2A-EKAREV-NLS	Kawabata et al.[62]	Addgene plasmid #173856
pPBbsr2-TSen	Chapnick et al.[35]	Addgene plasmid #209916
pPBbsr2-5102HRasCT(Picchu)	This paper	Addgene plasmid #209917
pCSIIbsr-Eevee-ROCK-NES	Hino et al.[26]	Addgene plasmid #209918
pPBPuro-miRFP703-eDHFR(69K6)-cRaf	This paper	Addgene plasmid #209919
pPBbleo-miRFP703-eDHFR(69K6)-cRaf	This paper	Addgene plasmid #209920
pPBbsr2-miRFP703-eDHFR(69K6)-cRaf	This paper	Addgene plasmid #209921
Software and algorithms		
Fiji	Schindelin et al.[63]	RRID:SCR_002285
Metamorph	Molecular Devices	RRID:SCR_002368
MATLAB	MathWorks	RRID:SCR_001622
Python	Python Software	Foundation RRID:SCR_008394